

# Geochemistry, Geophysics, Geosystems

## RESEARCH ARTICLE

10.1029/2020GC009559

### Key Points:

- Quantitative comparison methods in detrital studies are extended into two dimensions and applied to a zircon U-Pb and Hf global compilation
- Two-dimensional measures behave in a similar fashion to their one-dimensional counterparts in terms of sensitivity and consistency
- Detrital and igneous zircon records are similar for individual continents and reveal the unique Hf isotopic signature of Gondwana

### Supporting Information:

- Supporting Information S1
- Supporting Information S2
- Data Set S1
- Data Set S2

### Correspondence to:

K. E. Sundell,  
[sundell@arizona.edu](mailto:sundell@arizona.edu)

### Citation:

Sundell, K. E., & Saylor, J. E. (2021). Two-dimensional quantitative comparison of density distributions in detrital geochronology and geochemistry. *Geochemistry, Geophysics, Geosystems*, 22, e2020GC009559. <https://doi.org/10.1029/2020GC009559>

Received 23 NOV 2020

Accepted 26 JAN 2021

© 2021. American Geophysical Union.  
 All Rights Reserved.

## Two-Dimensional Quantitative Comparison of Density Distributions in Detrital Geochronology and Geochemistry

K. E. Sundell<sup>1,2</sup>  and J. E. Saylor<sup>3</sup> 

<sup>1</sup>Department of Geosciences, The University of Arizona, Tucson, AZ, USA, <sup>2</sup>Now at Department of Geosciences, Idaho State University, Pocatello, ID, USA, <sup>3</sup>Department of Earth, Ocean, and Atmospheric Sciences, University of British Columbia, Vancouver, BC, Canada

**Abstract** Detrital geochronology provides insight into a broad range of Earth Science questions. However, detrital zircon U-Pb age distributions are inherently univariate, and thus quantitative comparison methods are limited to one-dimension (1D) and subject to nonunique results due to overlapping age groups. We developed two-dimensional (2D) quantitative comparison measures for bivariate kernel density estimates (KDEs) and cumulative distribution functions (CDFs). These methods are extensions of 1D quantitative comparison measures commonly used in detrital geochronology: Similarity, Likeness, and Cross-correlation of KDEs and Kolmogorov-Smirnov (K-S) and Kuiper tests of CDFs. We demonstrate the efficacy of these methods by applying them to a global compilation of detrital and igneous zircon univariate U-Pb data ( $n = 767,660$ ) and bivariate U-Pb and Hf (i.e.,  $\epsilon\text{HfT}$ ) data ( $n = 114,311$ ) parsed geographically into eight continental landmasses demarcated by Paleozoic sutures. The 2D quantitative comparison measures behave in a similar fashion to their 1D counterparts in terms of sensitivity and consistency regardless of parameterization (e.g., kernel bandwidth and discretization interval). Results show that the detrital record reliably reflects the igneous record for both univariate U-Pb and bivariate  $\epsilon\text{HfT}$  distributions between 4,400 and 0 Ma. In contrast, 1D and 2D quantitative comparison results differ over the narrower Ediacaran-Cambrian time interval due to nonunique univariate zircon U-Pb age groups; the 2D quantitative results consistently identify continental landmasses involved in the formation of Gondwana. We implemented the 2D methods in a new MATLAB-based graphical user interface, *DZstats2D*, which is available as open-source code and as standalone applications for macOS and Windows.

## 1. Introduction

Detrital geochronology has transformed the way geologists approach many Earth Science questions. Research incorporating detrital geochronology is wide ranging, from standard application in studies of sediment provenance and dispersal patterns (e.g., Thomas et al., 2020), determination of the maximum depositional age of stratigraphy (e.g., Dickinson & Gehrels, 2009; Vermeesch, 2020), and reconstructing paleogeography and landscape evolution (e.g., Roberts, 2012), to recent novel applications in determining controls on paleoclimate modulations (e.g., McKenzie et al., 2016), placing temporal constraints on floral and faunal continental ecosystems (e.g., Tucker et al., 2013), and estimating the age of early hominins (e.g., Böhme et al., 2017).

Zircon is the mineral of choice in detrital geochronology as it is physically and chemically robust, refractory, can survive multiple erosional and/or tectonic cycles, and incorporates abundant U with little initial Pb (Cherniak et al., 1997; Speer, 1980; Stacey & Kramers, 1975). In addition to being a useful mineral for geochronology, zircon can also be paired with secondary information such as (U-Th)/He or fission track thermochronometry for determining thermal histories (e.g., Reiners, 2005; Stockli, 2005), trace element geochemistry for fingerprinting sediment sources (e.g., McKenzie et al., 2018; cf., Hoskin & Ireland, 2000), Hf analysis for understanding crustal evolution and the rate of crustal growth through time (e.g., Belousova et al., 2010; Roberts & Spencer, 2015), or physical characteristics of zircon such as grain roundness (Decou et al., 2013; Sundell et al., 2018) or grain size (Leary et al., 2020) for detailed analysis of sediment recycling and provenance.

Early interpretation of detrital zircon geochronology information began with bulk sample analysis of zircon concentrates (i.e., all of the zircons from a clastic sample dissolved and analyzed as a single analysis) for complementary visual assessment to geological observations (e.g., Tatsumoto & Patterson, 1964). Isotope-dilution thermal ionization mass spectrometry (ID-TIMS) and secondary ionization mass spectrometry (SIMS) enabled single-grain zircon analysis which led to early qualitative comparison of detrital zircon U-Pb age distributions (e.g., Schärer & Allègre, 1982). The advent and application of laser ablation-inductively coupled plasma-mass spectrometry (LA-ICP-MS) to detrital zircon U-Pb geochronology has dramatically increased the efficiency and rate of sample throughput, resulting in a punctuated increase in the number of ages typically measured for an individual sample ( $n$ ) from  $n \approx 60$  (e.g., Dodson et al., 1988) to  $n > 100$  in the early 2000s (Vermeesch, 2004), and more recently to  $n > 300$  for complex samples (e.g., Pullen et al., 2014; Sundell et al., 2020). The comparison of detrital zircon age distributions remained a primarily qualitative endeavor until the early 2000s (e.g., Gehrels et al., 1995). Since then, the research field has rapidly built in quantitative sophistication, with the development of pairwise comparison measures of age distributions (Amidon et al., 2005; Gehrels, 2000; Satkoski et al., 2013; Saylor et al., 2013; Saylor & Sundell, 2016; Tye et al., 2019; Vermeesch, 2018), to more advanced methods of forward and inverse detrital zircon U-Pb geochronology mixture modeling (e.g., Saylor et al., 2019; Sharman & Johnstone, 2017; Sundell & Saylor, 2017).

Detrital zircon U-Pb age distributions are univariate and thus are limited to one-dimensional (1D) quantitative comparison methods. Results of 1D comparisons are often nonunique due to overlapping or shared age groups between sample age distributions. We present two-dimensional (2D) quantitative comparison measures that are simple mathematical extensions of quantitative comparison measures commonly applied to univariate detrital zircon U-Pb age distributions. Specifically, we developed 2D Similarity, Likeness, and Cross-correlation of bivariate kernel density estimates (KDEs), and Kolmogorov-Smirnov (K-S) Test D and Kuiper Test V measures of bivariate cumulative distribution functions (CDFs). We demonstrate the utility of these methods with application to a global compilation of igneous and detrital zircon U-Pb and Hf data (Puetz & Condie, 2019). We developed the 2D methods in MATLAB and provide a new software package, *DZstats2D*, as open-source code and as standalone graphical user interfaces for macOS and Windows available at [github.com/kurtsundell/DZstats2D](https://github.com/kurtsundell/DZstats2D) along with all of the data discussed in this contribution.

## 2. Data Visualization

### 2.1. Univariate Data Visualization

Univariate detrital age distributions (i.e., age only) can be visualized in a variety of ways. The simplest visualizations of such data are univariate scatter plots (Figure 1a) and binned histograms (Figure 1b). More commonly in detrital geochronology, univariate age distributions are visualized as probability density plots (PDPs) or KDEs (Figure 1c), or CDFs (Figure 1d).

PDPs are discrete distributions that estimate an age distribution's probability density function (PDF). PDPs are calculated from  $n$  observations as

$$f(x) = \frac{1}{n} \sum_{i=1}^n f_i(x), \quad (1)$$

where  $n$  is the number of ages and each age,  $f_i(x)$ , is represented by a Gaussian function

$$f_i(x) = \frac{1}{\sigma_i \sqrt{2\pi}} \exp \left[ -\frac{1}{2} \times \left( \frac{x - \mu_i}{\sigma_i} \right)^2 \right], \quad (2)$$

where  $\mu_i$  is the grain age,  $\sigma_i$  is the corresponding analytical uncertainty, and  $i$  is a single analysis (Miller, 2014; Pearson, 2011; Saylor & Sundell, 2016). PDPs tend to oversmooth the older age fraction of detrital distributions because uncertainty generally scales with age and the individual Gaussian curves are wider and lower amplitude for older ages.

KDEs are another way to estimate a sample age distribution's PDF, calculated as

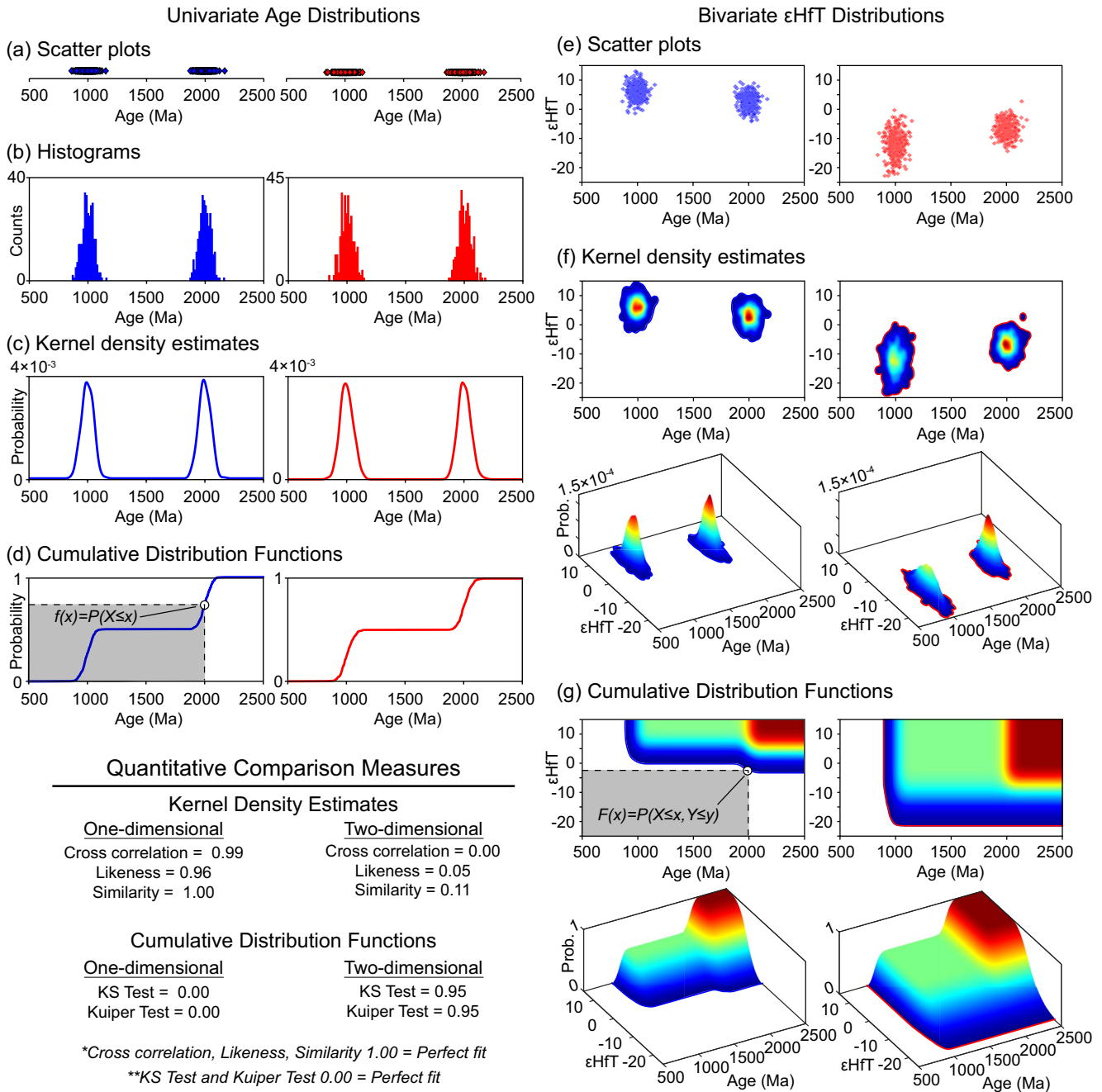


**Figure 1.** Motivation for 2D quantitative comparison. Univariate age distributions shown as (a) scatter plots, (b) histograms, (c) kernel density estimates, and (d) cumulative distribution functions. Bivariate εHfT distributions shown as (e) scatter plots, (f) kernel density estimates with 2D view (upper) and 3D view (lower), (g) cumulative distribution functions with 2D view (upper) and 3D view (lower). The bivariate data have the same ages as the univariate data, but the quantitative comparison results are significantly different in 1D and 2D.

$$\hat{f}_h(x) = \sum_{i=1}^n \frac{1}{nh} K\left[\frac{x - \mu_i}{h}\right], \quad (3)$$

where  $n$  is the number of observations,  $h$  is the kernel bandwidth,  $K$  is the kernel function (typically a Gaussian curve, but also can be a triangle, boxcar, etc.), and  $\mu_i$  is the grain age (Silverman, 1986; Vermeesch, 2012). KDEs do not incorporate analytical uncertainty, as the Gaussian kernel bandwidth is set arbitrarily or

determined using sample density optimization methods (e.g., Botev et al., 2010; Vermeesch, 2018). Conversely to PDPs, KDEs tend to oversmooth the younger fraction of detrital age distributions.

Empirical CDFs are cumulative sum step functions that increase by  $1/n$  for every observation along  $x$  from 0 to 1 along  $y$  (Figure 1d). The  $y$ -axis value of a CDF is the fractional representation of probability that observations in a sample that are less than or equal to the corresponding  $x$ -axis value such that

$$f_i(x) = P(X \leq x), \quad (4)$$

where  $f_i$  is the function of  $x$  as an empirical CDF,  $X$  is a random value or observation in  $f_i$ , and  $P$  is the probability that  $X$  will have a value less than or equal to  $x$  (Figure 1d). Similar to KDEs, CDFs do not incorporate sample uncertainty.

## 2.2. Bivariate Data Visualization

Bivariate data can also be visualized in a number of ways. The most common way to visualize bivariate data is with bivariate scatter plots (Figure 1e). Unfortunately, scatter plots do not give a good sense of data density, which is critical information for interpretations of detrital distributions. Bivariate KDEs are a practical and common way to visualize data density that have been previously applied to zircon U-Pb and Hf data (e.g., Andersen, 2014; Roberts & Spencer, 2015; Spencer et al., 2019). Bivariate KDEs typically take the form of color-coded intensity plots, with the three-dimensional (3D) density volume viewed parallel to a  $z$ -axis (Figure 1f). Bivariate KDEs can be constructed in a similar fashion to univariate KDEs (Silverman, 1986) where each data point is converted into a 3D Gaussian volume, summed, and normalized such that the density distribution integrates to 1. A computationally efficient way to construct bivariate KDEs as implemented here involves first performing a discrete cosine transform of the bivariate data (Ahmed et al., 1974) onto a square grid based in a factor of 2 (e.g.,  $2^9 \times 2^9 = 512 \times 512$ ); multiplying the resulting bivariate matrix by a Gaussian function with specified kernel bandwidths in both the  $x$  and  $y$  directions; performing an inverse discrete cosine transform of the Gaussian-scaled matrix, and normalizing such that the resulting volume integrates to 1. As with a univariate KDE, the Gaussian kernel bandwidth can be set arbitrarily or determined via optimization based on sample density (Botev et al., 2010). A common rule of thumb is to set the kernel bandwidths based on typical analytical uncertainty levels (e.g., 1%–2% for U-Pb, 0.5–1  $\epsilon$  units for Lu-Hf, at  $1\sigma$ ).

CDFs can also be visualized in bivariate space. An efficient way to construct a bivariate CDF is to first construct a bivariate KDE, then calculate the cumulative sum in both the  $x$ -axis and  $y$ -axis directions (Figure 1g). This can also be done by taking the cross product of cumulative sums in the  $x$ - and  $y$ -axis directions. The result is a volume with  $z$ -axis values that monotonically increase to 1 in a shared corner of  $x$ -axis and  $y$ -axis space (Figure 1g). The bivariate CDF may differ depending on which  $x$ - $y$  quadrant (I–IV) is considered and therefore can be defined in four ways (Peacock, 1983; Press & Teukolsky, 1988):

$$F_1(X, Y) = P(X \leq x, Y \leq y) \text{ (quadrant I, shown in Figure 1g)}, \quad (5)$$

$$F_2(X, Y) = P(X > x, Y \leq y) \text{ (quadrant II)}, \quad (6)$$

$$F_3(X, Y) = P(X > x, Y > y) \text{ (quadrant III)}, \quad (7)$$

$$F_4(X, Y) = P(X \leq x, Y > y) \text{ (quadrant IV)}. \quad (8)$$

## 3. Quantitative Comparison

### 3.1. 1D Quantitative Comparison

Several methods have been developed as relative measures of similarity and dissimilarity in detrital geochronology. Because univariate PDPs and KDEs are continuous functions, two functions  $f(x)$  and  $g(x)$  can

be quantitatively compared by discretizing them at the same interval (e.g., 1 Myr steps) over the same age range (e.g., 500–2,500 Ma; Figures 1b and 2a–2b). Figures 2a–2b shows two KDEs with a coarse 40 Myr discretization interval (i.e., one  $y$  axis value for every 40 Myr along  $x$ ). A simple way to compare these distributions is to calculate their similarity. Similarity in 1D ( $S_{1D}$ ) is the same as the Bhattacharya Coefficient between two discrete probability distributions (Bhattacharya, 1943) and was introduced to detrital geochronology by Gehrels (2000). Similarity is calculated by taking the sum of geometric mean of each pair of  $y$  axis values along  $x$ :

$$S_{1D} = \sum \sqrt{f(x) \times g(x)}. \quad (9)$$

Here, 1 is perfectly similar and 0 perfectly dissimilar. The individual geometric mean calculations can also be plotted before summing for a visual representation of  $S_{1D}$  with higher  $y$ -axis values corresponding to where  $f(x)$  and  $g(x)$  are similar (Figure 2c). Another way to compare two univariate PDPs or KDEs is to calculate Mismatch (Amidon et al., 2005). Mismatch is the sum the absolute difference of each pair of  $y$ -axis values along  $f(x)$  and  $g(x)$  divided by 2:

$$M_{1D} = \sum \frac{|f(x) - g(x)|}{2}, \quad (10)$$

where 1 is perfectly dissimilar and 0 is perfectly similar. As above, the individual  $M_{1D}$  calculations along  $x$  can be plotted before summing to produce a visual representation showing where  $f(x)$  and  $g(x)$  are dissimilar (Figure 2d). Likeness (Satkoski et al., 2013) is the complement to Mismatch and calculated as

$$L_{1D} = 1 - M_{1D}, \quad (11)$$

where 0 is perfectly dissimilar and 1 is perfectly similar, as with  $S_{1D}$  above. A fourth way to quantitatively compare two PDPs or KDEs is to calculate the coefficient of determination. Here, the Cross-correlation coefficient of univariate detrital data ( $R^2_{1D}$ , Saylor et al., 2013) is calculated as

$$R^2_{1D} = \left[ \frac{\sum [(f(x) - \bar{f}) \times (g(x) - \bar{g})]}{\sqrt{\sum (f(x) - \bar{f})^2 \times \sum (g(x) - \bar{g})^2}} \right]^2 \quad (\text{Figure 2e}). \quad (12)$$

Relative measures of dissimilarity can be calculated from two CDFs (Figure 1d) with the Komolgorov-Smirnov (K-S) Test D statistic (Massey, 1951) and the Kuiper Test V statistic (Kuiper, 1960). The K-S Test D statistic is the maximum absolute difference between two CDFs

$$D_{1D} = \max(|\text{CDF1} - \text{CDF2}|). \quad (13)$$

The Kuiper Test V statistic is the sum of the maximum differences between CDF1 and CDF2 and vice versa:

$$V_{1D} = \max(\text{CDF1} - \text{CDF2}) + \max(\text{CDF2} - \text{CDF1}). \quad (14)$$

For both  $D_{1D}$  and  $V_{1D}$ , 1 is perfectly dissimilar and 0 is perfectly similar. K-S Test and Kuiper Test  $D_{1D}$  and  $V_{1D}$  can be used to produce  $p$ -values. However,  $p$ -values represent statistical hypothesis tests that are poorly suited for quantitative analysis of detrital data (Vermeesch, 2013, their Appendix B). Specifically, calculation of  $p$ -values in detrital geochronology produces too many Type-I errors (rejecting a true null hypothesis) and Type-II errors (accepting of a false null hypothesis) because they are highly sensitive to the number of ages in a distribution ( $n$ ) used to produce the CDFs, and also due to mixing  $n$  with “effect size,” that is, the degree to which the null hypothesis is false (Cohen, 1977; Vermeesch, 2013). Thus,  $p$ -values are unsuitable for comparison of detrital age distributions and should not be used as relative measures of dissimilarity (Saylor & Sundell, 2016; Vermeesch, 2013). Furthermore,  $p$ -values are fraught with issues and have been historically misused across the physical sciences (see recent review in Hubbard, 2019 and summary of best practices for  $p$ -values in Wasserstein et al., 2019).



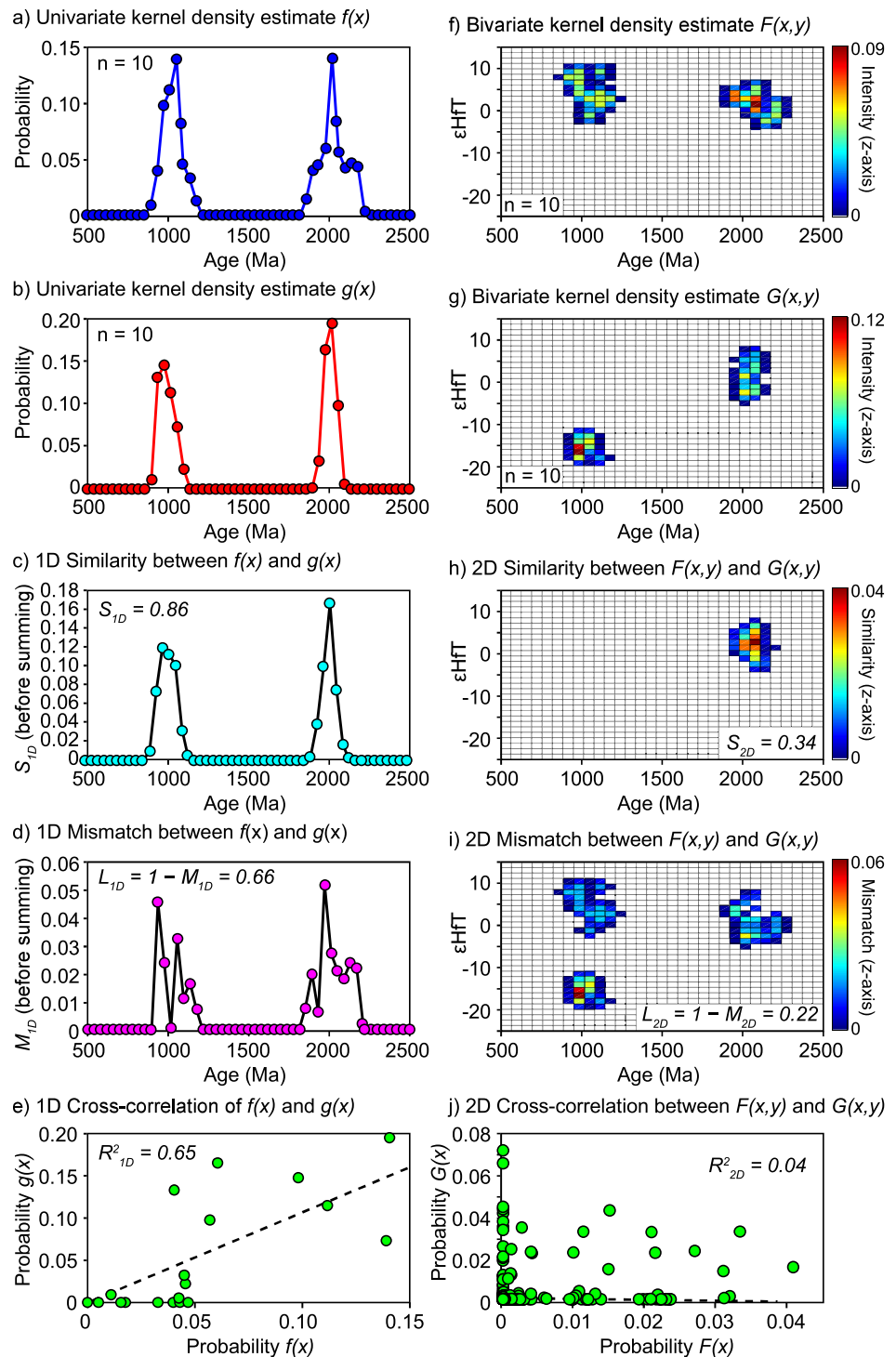


**Figure 2.** 1D and 2D quantitative comparison methods for univariate and bivariate kernel density estimates (KDEs). ((a)–(b)) Example KDEs  $f(x)$  and  $g(x)$ . (c) Intermediate step in calculating Similarity before summing. (d) Intermediate step in calculating Mismatch. (e) Cross plot of each pair of points along the x-axis from  $f(x)$  and  $g(x)$ ; linear regression of these values is used to calculate the coefficient of determination, Cross-correlation. ((f)–(j)) Bivariate counterparts to ((a)–(e)). Note that the 1D quantitative comparisons yield very similar results and the 2D comparisons yield very dissimilar results, despite sharing common ages. The lowest values of the colorbars for parts f–i are white in order to clip the bivariate plots at the 98% from peak density level.

### 3.2. 2D Quantitative Comparison

Each of the 1D measures of similarity and dissimilarity can be modified to handle bivariate data. Quantitative comparison of the univariate and bivariate distributions in Figure 1 motivates the development of 2D quantitative comparison. Specifically, the 1D measures consistently show the distributions are nearly identical (Figures 1a–1d). However, 2D measures reveal these same data are indeed quite dissimilar with consideration of a second dimension (Figures 1e–1g).

As with univariate distributions, bivariate distributions can be represented as discretized functions. Figures 2f–2g shows two coarsely discretized bivariate kernel density estimates  $F(x,y)$  and  $G(x,y)$  with data points every 125 Myr on the  $x$ -axis and 2.5  $\epsilon$  units on the  $y$ -axis (as determined from discretization on a  $16 \times 16$  grid with an  $x$ -axis range from 500 to 2,500 Ma and  $y$ -axis range from  $-25$  to 15  $\epsilon$  units). Similarity can be extended to 2D by calculating the sum of geometric mean of each value of a square  $x \times y$  matrix:

$$S_{2D} = \sum \sqrt{F(x,y) \times G(x,y)} \quad (\text{Figures 2f–2h}). \quad (15)$$

Here, each pair of values along both the  $x$ -axis and  $y$ -axis directions produces a third matrix of values that may be plotted as a 2D intensity plot of Similarity values which highlight where two 2D density distributions are similar (Figure 2h), which when integrated produces  $S_{2D}$ .

Mismatch is extended to 2D as

$$M_{2D} = \sum \frac{|F(x,y) - G(x,y)|}{2} \quad (\text{Figure 2i}). \quad (16)$$

Here, half of the absolute difference is calculated for each  $x \times y$  value of two bivariate KDEs  $F(x,y)$  and  $G(x,y)$  and summed together to produce  $M_{2D}$ . As with the  $S_{2D}$  calculation, an intermediate matrix of values is produced and can be plotted before summing; this plot shows where  $F(x,y)$  and  $G(x,y)$  are dissimilar (Figure 2i), which when summed together gives  $M_{2D}$ . Similarity and Mismatch are unique in that they can be visualized as 2D intensity plots of similarity and dissimilarity, respectively, whereas the following 2D quantitative measures do not lend themselves to this type of visualization because they either involve calculations that are already summed to a single value (e.g.,  $L_{2D}$ ) or involve multiple summations (e.g.,  $R^2_{2D}$ ). For example, Likeness is converted to 2D as

$$L_{2D} = 1 - M_{2D}. \quad (17)$$

Here,  $L_{2D}$  cannot be visualized as a 2D intensity plot of correspondence because  $M_{2D}$  is already reduced to a single value. Cross-correlation for bivariate data is calculated as

$$R^2_{2D} = \left[ \frac{\sum [(F(x,y) - \bar{F}) \times (G(x,y) - \bar{G})]}{\sqrt{\sum (F(x,y) - \bar{F})^2 \times \sum (G(x,y) - \bar{G})^2}} \right]^2 \quad (\text{Figure 2j}). \quad (18)$$

The K-S Test can be modified to calculate quantitative comparison of bivariate CDFs (e.g., Peacock, 1983). The D statistic is calculated in a similar way to the 1D scenario where

$$D_{2D} = \max(|\text{CDF1} - \text{CDF2}|), \quad (19)$$

for all pairwise values of two bivariate CDFs (Figure 1g). One critical difference is that every bivariate CDFs can be defined in four different ways by summing to one of four different quadrants (see Section 2.2, Figure 1g). We follow the approach of Peacock (1983) where the maximum difference between two bivariate CDFs is calculated four times, each time summing to a different quadrant, calculating the K-S Test D value and reporting the maximum absolute difference of all four calculations as  $D_{2D}$ . The Kuiper Test is converted to 2D in a similar fashion as the sum of the maximum differences between CDF1 and CDF2 and vice versa:

$$V_{2D} = \max(\text{CDF1} - \text{CDF2}) + \max(\text{CDF2} - \text{CDF1}), \quad (20)$$

where like the 2D K-S Test, it considers all four possible quadrant sums. For similar reasons as outlined above,  $p$ -values are not considered here for the K-S and Kuiper tests, although they have been developed for the K-S Test (Peacock, 1983).

### 3.3. Multidimensional Scaling

Pairwise quantitative comparison matrices can be visualized using multidimensional scaling (MDS) in a similar fashion as is done for traditional 1D age distributions (e.g., Vermeesch, 2013). MDS facilitates visualization of pairwise comparison matrices by transforming sample dissimilarity into distance on a Cartesian plot in  $N$  dimensions. Similarity, Likeness, and Cross-correlation all yield “similarity” matrices, which can be converted into sample dissimilarity by subtracting from 1 (e.g.,  $1 - S_{2D}$ ). Both the K-S Test and Kuiper Test produce sample dissimilarity. Transformation of dissimilarity to distance in MDS is accomplished through iterative rearrangement in Cartesian space, seeking to minimize the misfit (termed “stress”) between the distance and disparity (where disparity is a linear transformation of distance in the case of metric MDS or the ordination in the case of nonmetric MDS). Stress is normalized by the sum of the squares of the interpoint distances. Low stress (e.g.,  $<0.1$ ) indicates a reasonable transformation (Kruskal, 1964; Vermeesch, 2013). One of the most commonly used methods to accomplish this task is Kruskal’s method of nonmetric MDS (Kruskal, 1964). Here, a pairwise dissimilarity matrix is converted to distance through isotonic regression, that is, fitting a monotonically increasing line through the ranked matrix values, such that the Euclidean distances have approximately the same rank order as the corresponding dissimilarities; the transformed values are disparities. Results are represented as points in Cartesian space with greater distance corresponding to greater dissimilarity.

## 4. Application to a Global Compilation of Zircon U-Pb and Hf Data

We applied 1D and 2D quantitative comparison methods to the global zircon U-Pb and Hf data compilation of Puetz and Condie (2019). We used a modified version of this data compilation that was parsed geographically based on Paleozoic suture locations from Domeier and Torsvik (2014) that includes eight continental landmasses: Africa, Antarctica, Australia, Asia, Baltica, North America, Peri-Gondwana, and South America (Figure 3). Africa includes the Arabian Peninsula. Asia was divided along the Paleo-Tethys suture between Peri-Gondwana and surrounding Eurasian terranes (Metcalf, 2013), and includes Siberia, Tarim, North China, South China, and terranes in Central Asia. Australia includes the southeastern Asian terranes. Baltica is separated from Asia along the eastern Ural Mountains. Baltica and Asia were separated from Peri-Gondwana terranes along the Paleo-Tethys suture. North America is separated from Peri-Gondwana terranes along the Iapetan suture. India is included with Peri-Gondwana. South America includes the Peri-Gondwana terranes of Mexico.

After grouping the data geographically, the global compilation was subdivided into its igneous zircon and detrital zircon contributions, and then further subdivided into univariate contributions of U-Pb data only ( $n = 767,660$ ) and bivariate contributions of paired U-Pb and Hf data ( $n = 114,311$ ). This parsing produced 32 groups of data: two primary data sets of univariate (U-Pb) and bivariate (U-Pb and Hf) data, each with eight spatial groups of igneous zircon and detrital zircon data.

Hf isotope geochemical data are reported in  $\epsilon$  units in reference to the chondritic uniform reservoir (CHUR) and expressed as  $\epsilon\text{HfT}$  where

$$\epsilon\text{HfT} = \left( \frac{\frac{176\text{Hf}}{177\text{Hf}} - \frac{176\text{Lu}}{177\text{Hf}} \times e^{\lambda T - 1}}{C_{\text{Hf,CHUR}(0)} - C_{\text{Lu,CHUR}(0)} \times e^{\lambda T - 1}} - 1 \right) \times 10,000, \quad (21)$$



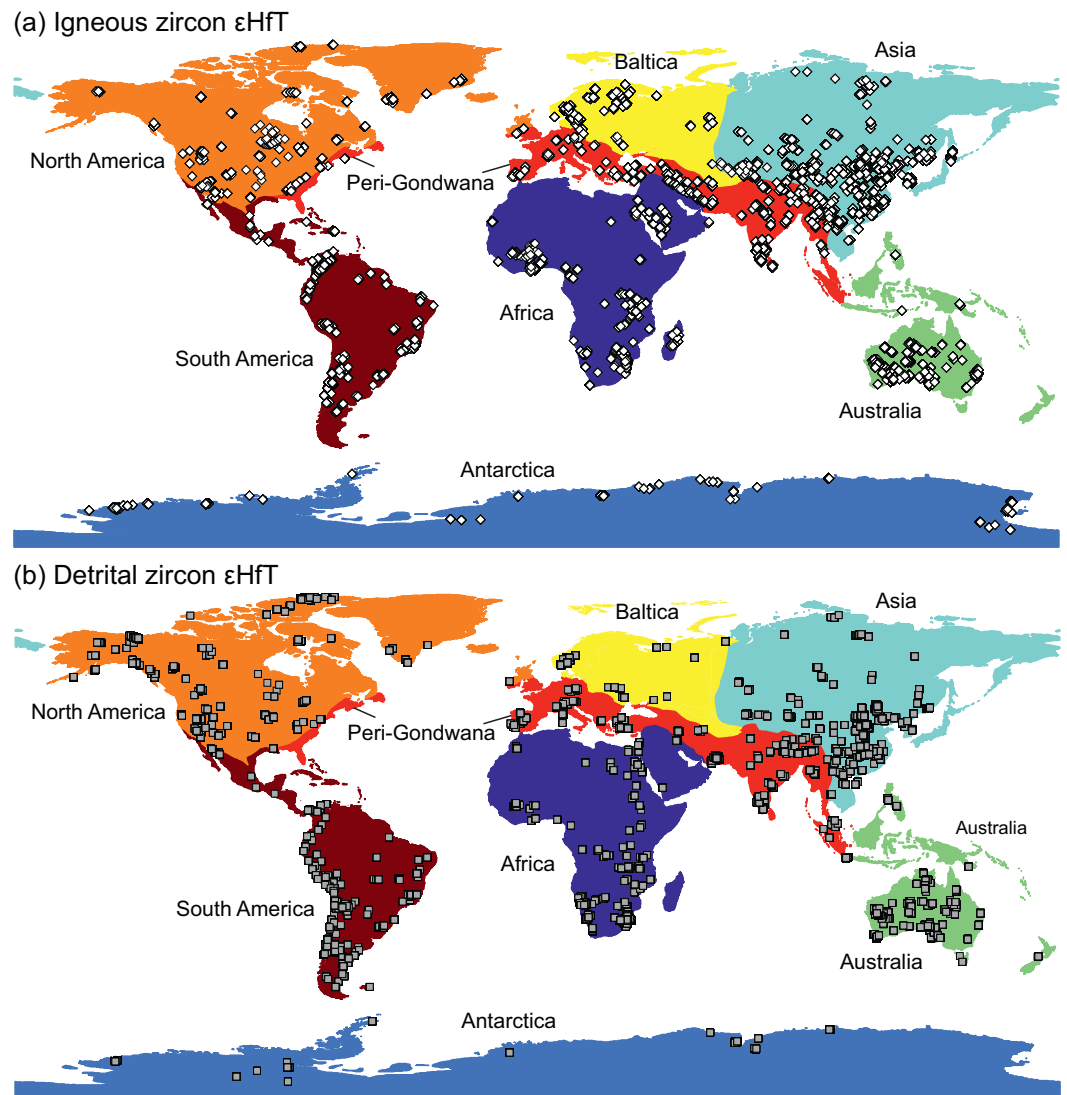


**Figure 3.** Spatial distribution of (a) igneous zircon and (b) detrital zircon paired U-Pb and initial Hf ( $\epsilon\text{HfT}$ ) compiled in Puetz and Condie (2019). Sample locations are separated into paleocontinents based on Paleozoic terrane sutures from Domeier and Torsvik (2014).

where  $^{176}\text{Hf}/^{177}\text{Hf}$  and  $^{176}\text{Lu}/^{177}\text{Hf}$  are measured isotopic values of zircon;  $\lambda$  is the  $^{176}\text{Lu}$   $\beta$ -decay rate of  $1.867 \times 10^{-5} \text{ Myr}^{-1}$  (Söderlund et al., 2004);  $C_{\text{Hf,CHUR}}(0)$  and  $C_{\text{Lu,CHUR}}(0)$  are present day  $^{176}\text{Hf}/^{177}\text{Hf}$  and  $^{176}\text{Lu}/^{177}\text{Hf}$  CHUR of 0.282772 and 0.0332, respectively (Griffin et al., 2000); and  $T$  is the zircon U-Pb crystallization age. This represents parts per 10,000 deviation from CHUR at the time of zircon crystallization ( $T$ ). The depleted mantle array is calculated using an initial  $^{176}\text{Hf}/^{177}\text{Hf}$  value of 0.283225 and initial  $^{176}\text{Lu}/^{177}\text{Hf}$  value of 0.0383 (Vervoort & Blichert-Toft, 1999).

Below, we will first demonstrate the 2D calculations by working through a simple example using the igneous and detrital zircon bivariate  $\epsilon\text{HfT}$  data. Then we perform sensitivity testing of the individual quantitative measures in 1D and 2D using the zircon  $\epsilon\text{HfT}$  considered in its univariate (i.e., U-Pb only) and bivariate (i.e., U-Pb and Hf) components. Finally, we use the complete data sets of univariate U-Pb data ( $n = 767,660$ ) and bivariate  $\epsilon\text{HfT}$  data ( $n = 114,311$ ) to address two example geologic questions: (1) How similar are the detrital zircon and igneous zircon geochronological and geochemical records? (2) Is the Ediacaran-Cambrian  $\epsilon\text{HfT}$  negative isotopic excursion a global signal?

#### 4.1. Simple Example

To demonstrate how the 2D quantitative comparison measures are calculated, let us consider two data sets, the igneous zircon and detrital zircon  $\epsilon\text{HfT}$  data from Africa. We first generate two bivariate KDEs that range from 0 to 4,400 Ma on the  $x$ -axis and  $-40$  to 20  $\epsilon\text{HfT}$  on the  $y$ -axis with extremely coarse discretization over a 4-by-4 grid where

$$F = \begin{bmatrix} 0.0041 & 0.0025 & 0.0000 & 0.0000 \\ 0.0664 & 0.0200 & 0.0093 & 0.0013 \\ 0.1409 & 0.1682 & 0.2412 & 0.0823 \\ 0.2386 & 0.0153 & 0.0089 & 0.0011 \end{bmatrix}$$

and

$$G = \begin{bmatrix} 0.0040 & 0.0003 & 0.0001 & 0.0000 \\ 0.0531 & 0.0148 & 0.0100 & 0.0008 \\ 0.3110 & 0.1535 & 0.1616 & 0.0529 \\ 0.1977 & 0.0337 & 0.0057 & 0.0008 \end{bmatrix}.$$

$S_{2D}$  is calculated first with an intermediate step that yields a matrix of values where  $S_{2D}$  before summing is

$$S_{2D,\text{intermediate}} = \begin{bmatrix} 0.0041 & 0.0008 & 0.0000 & 0.0000 \\ 0.0594 & 0.0172 & 0.0096 & 0.0010 \\ 0.2093 & 0.1607 & 0.1974 & 0.0659 \\ 0.2172 & 0.0227 & 0.0071 & 0.0010 \end{bmatrix}.$$

which when summed yields  $S_{2D}$  of 0.97. Mismatch in 2D also contains an intermediate step where  $M_{2D}$  of  $F$  and  $G$  (before summing) is

$$M_{2D,\text{intermediate}} = \begin{bmatrix} 0.0000 & 0.0011 & 0.0000 & 0.0000 \\ 0.0066 & 0.0026 & 0.0026 & 0.0002 \\ 0.0850 & 0.0073 & 0.0398 & 0.0147 \\ 0.0204 & 0.0092 & 0.0016 & 0.0001 \end{bmatrix}.$$

Summing this matrix produces  $M_{2D}$  of 0.19; subtracting from 1 (i.e., plugging into Equation 17) yields  $L_{2D} = 0.81$ .

Calculating the Cross-correlation coefficient of  $F$  and  $G$  requires vectorizing (i.e., reshaping) each matrix into 1D arrays where

$$F_{\text{vectorized}} = [0.0041 \ 0.0664 \ 0.1409 \ 0.2386 \ 0.0025 \ \dots \ 0.0823 \ 0.0011]$$

and

$$G_{\text{vectorized}} = [0.0040 \ 0.0531 \ 0.3110 \ 0.1977 \ 0.0003 \ \dots \ 0.0529 \ 0.0008].$$

Application of Equation 18 yields a Cross-correlation coefficient of 0.71.

The  $S_{2D}$  and  $L_{2D}$  measures can also be calculated by vectorizing  $F$  and  $G$  and will produce an identical result to the examples shown above. However, while vectorizing is a slightly more computationally efficient way to calculate  $S_{2D}$  and  $L_{2D}$ , there is the added benefit of the intermediate steps of calculating  $S_{2D}$  and  $M_{2D}$  which can be plotted to show where  $F$  and  $G$  are similar (Figure 2h) or dissimilar (Figure 2i), respectively.

Following from the same example of coarsely gridded igneous and detrital zircon  $\epsilon\text{HfT}$  data from Africa, bivariate CDFs that sum to 1 in the first quadrant of  $F$  and  $G$  are

$$F = \begin{bmatrix} 0.4499 & 0.6560 & 0.9154 & 1.0000 \\ 0.4459 & 0.6494 & 0.9088 & 0.9934 \\ 0.3795 & 0.5630 & 0.8131 & 0.8964 \\ 0.2386 & 0.2539 & 0.2628 & 0.2639 \end{bmatrix}$$

and

$$G = \begin{bmatrix} 0.5658 & 0.7681 & 0.9455 & 1.0000 \\ 0.5618 & 0.7638 & 0.9411 & 0.9956 \\ 0.5086 & 0.6959 & 0.8632 & 0.9169 \\ 0.1977 & 0.2314 & 0.2371 & 0.2379 \end{bmatrix}.$$

Taking the difference between  $F$  and  $G$  gives

$$F - G = \begin{bmatrix} -0.1158 & -0.1121 & -0.0301 & 0.0000 \\ -0.1159 & -0.1145 & -0.0324 & -0.0022 \\ -0.1292 & -0.1329 & -0.0501 & -0.0204 \\ 0.0409 & 0.0225 & 0.0258 & 0.0260 \end{bmatrix},$$

and vice versa gives

$$G - F = \begin{bmatrix} 0.1158 & 0.1121 & 0.0301 & 0.0000 \\ 0.1159 & 0.1145 & 0.0324 & 0.0022 \\ 0.1292 & 0.1329 & 0.0501 & 0.0204 \\ -0.0409 & -0.0225 & -0.0258 & -0.0260 \end{bmatrix}.$$

Following Equation 19, the maximum of the latter two matrices is the K-S Test  $D_{2D}$  value of 0.13. Following Equation 20, the Kuiper Test  $V_{2D}$  value is the sum of the maximum of each of the latter two matrices and produces a result of 0.17. Again note, because there are three alternate quadrants, this value is not necessarily the largest, and hence may not be the appropriate maximum difference between the bivariate CDFs (Peacock, 1983). For example, if we sum to the corner of the fourth quadrant,  $F$  and  $G$  would be

$$F = \begin{bmatrix} 0.0041 & 0.0066 & 0.0066 & 0.0066 \\ 0.0705 & 0.0930 & 0.1023 & 0.1036 \\ 0.2114 & 0.4021 & 0.6525 & 0.7361 \\ 0.4499 & 0.6560 & 0.9154 & 1.0000 \end{bmatrix},$$

and

$$G = \begin{bmatrix} 0.0040 & 0.0043 & 0.0044 & 0.0044 \\ 0.0572 & 0.0723 & 0.0823 & 0.0831 \\ 0.3681 & 0.5367 & 0.7084 & 0.7621 \\ 0.5658 & 0.7681 & 0.9455 & 1.0000 \end{bmatrix}.$$

In this scenario,  $D_{2D} = 0.16$ , and  $V_{2D}$  is the same as before, 0.17. To reiterate, to find the maximum difference between two bivariate CDFs, four separate K-S Tests and Kuiper Tests must be done with the largest value reported based on bivariate CDFs that sum to 1 in each of the four quadrants (Peacock, 1983).

#### 4.2. Sensitivity Testing

We use the empirical data from the global zircon U-Pb and Hf compilation of Puetz and Condie (2019) to test the sensitivity of the 1D and 2D quantitative measures. From the 114,313 pairs of  $\epsilon\text{HfT}$  data, two samples comprising  $n = 50,000$  each were selected without replacement. We then randomly selected sets

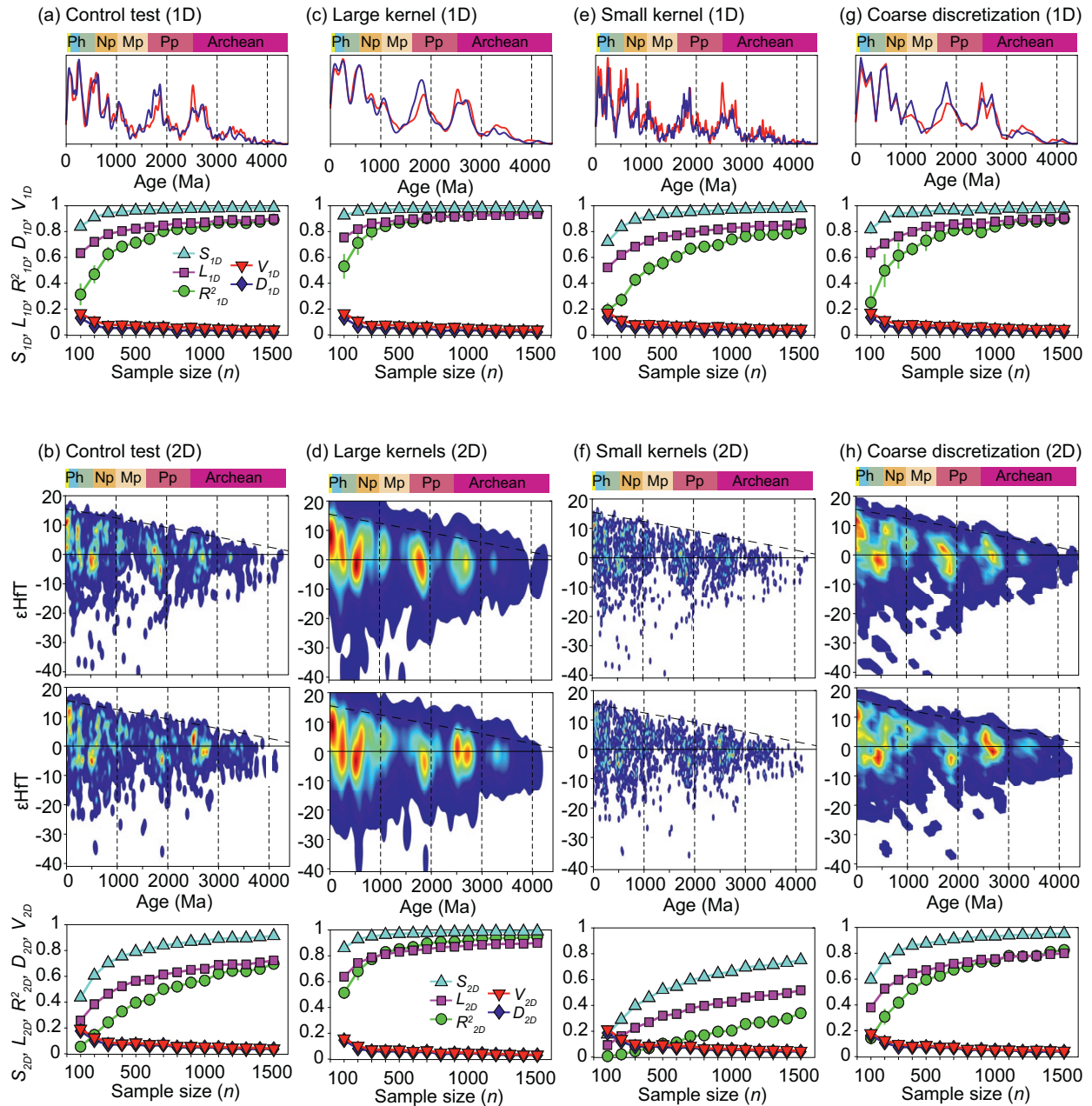


**Figure 4.** Sensitivity testing of 1D and 2D quantitative comparison methods. (a)–(b) Control test incorporating kernel bandwidths of 20 Myr and 1  $\epsilon$  unit and discretization intervals of (a) 1 Myr for univariate distributions and (b) a  $512 \times 512$  grid for bivariate distributions. (c)–(d) Test results with larger kernel bandwidths of 50 Myr and 4  $\epsilon$  units. (e)–(f) Test results with smaller kernel bandwidths of 10 Myr and 0.5  $\epsilon$  units. (g)–(h) Coarse discretization interval test results with (g) 100 Myr for univariate distributions and (h) a  $32 \times 32$  grid for bivariate distributions.

of  $n = 100, 200 \dots 1,500$  from each data set 10 times and compared them using each quantitative measure. Results are reported as median  $\pm 1\sigma$  standard deviation for each sample size,  $n$  (Figure 4). For simplicity, the 1D and 2D tests are based on the same data two samples, with univariate distributions constructed from the bivariate data without consideration of the Hf component.

We conducted four tests in 1D and 2D. Our initial test serves as a control for varying two parameters: kernel bandwidth (i.e., width of individual Gaussian curves used for each data point) and discretization interval (i.e., spacing in the  $x$  and  $y$  directions). The control test used kernel bandwidths of 20 Myr and 1  $\epsilon$  unit and discretization intervals of 1 Myr for univariate distributions (Figure 4a) and a  $512 \times 512$  grid for bivariate

distributions (Figure 4b). We vary one parameter at a time for the following tests. The second test includes larger kernel bandwidths of 50 Myr and 4  $\epsilon$  units (Figures 4c–4d). The third test includes smaller kernel bandwidths of 10 Myr and 0.5  $\epsilon$  units (Figures 4e–4f). The fourth test incorporates very coarse discretization intervals of 100 Myr for univariate distributions (Figure 4g) and a  $32 \times 32$  grid for bivariate distributions (Figure 4h).

Results show common features among all tests. In all cases, and both for 1D and 2D, increased sample size produces more similar results shown by increasing Similarity, Likeness, and Cross-correlation values, and decreasing K-S Test and Kuiper Test values (Figure 4). As expected, the K-S and Kuiper tests do not show any change in 1D because the varied parameters do not change how univariate CDFs are constructed; in 2D the results do depend on the parameterizations tested (because the bivariate CDFs are calculated from the bivariate KDEs) and show no major changes among the four tests (Figure 4).

Another common feature among all results is the relative sensitivity to sample size (i.e., the measure that shows the largest range). Cross-correlation shows the greatest impact of sample size for both univariate and bivariate data (Figure 4). Similarity and Likeness have a wider range of sensitivity to sample size (i.e., covers a wider range between 0 and 1) in 2D than in 1D, whereas Cross-correlation has a wider range in 1D; the K-S Test and Kuiper Test show lower sensitivity than the other measures and are roughly equally sensitive in both 1D and 2D. Likeness is more sensitive than Similarity in 1D (Figures 4a, 4c and 4e, 4g) and roughly equally sensitive in 2D (Figures 4b, 4d and 4f, 4h). The K-S Test and Kuiper Test similarly show the lowest range of sensitivity (Figure 4).

Although there are many common features among the results, the key controlling parameter appears to be kernel size. As discussed by Vermeesch (2018) for 1D quantitative comparisons, larger kernel bandwidths produce more similar results, particularly for Likeness and Cross-correlation, whereas smaller kernel bandwidths produce less similar results; the latter has a more dramatic effect on the resulting systematic shift toward lower similarity. The discretization interval results (Figures 4g–4h) show little effect compared to the control test (Figures 4a–4b) with the exception that Cross-correlation becomes more similar more quickly with the coarse discretization than in the control case. The K-S and Kuiper tests appear to converge in 2D for the tests incorporating a large kernel (Figures 4c–4d) and coarse discretization (Figures 4g–4h). Despite these differences in parameterization, the quantitative comparisons are largely consistent regardless of which measure is used (Figure 4).

### 4.3. How Similar are the Detrital Zircon and Igneous Zircon Records?

The first geologic application is a comparison of igneous and detrital zircon data for the complete data sets of univariate U-Pb data ( $n = 767,660$ ) and bivariate  $\epsilon$ HfT data ( $n = 114,311$ ) over the full temporal range (i.e., 4,400 to 0 Ma) of the data compilation of Puetz and Condie (2019). The goal is to test how representative the detrital zircon record is of the igneous zircon record for major continental landmasses (Figure 3). Figure 5 shows each of the 32 groups of data described above plotted from 4,400 to 0 Ma with univariate zircon U-Pb age distributions shown as black lines and bivariate  $\epsilon$ HfT distributions shown as colored intensity plots. In general, the density modes of univariate distributions (peaks of black lines) and bivariate distributions (warm colors) occur over similar time intervals.

Quantitative comparison results are consistent with visual assessment for both univariate and bivariate distributions. The 16 groups of each of the two major groups of data (univariate and bivariate) were compared in a pairwise fashion using each of the five quantitative methods described above. Simplified results of the quantitative comparisons are individually color-coded based in Figure 6 with cooler colors indicating more similar density distributions and warmer colors indicating less similar density distributions (complete pairwise comparison matrices for each test are reported in the Supporting Information). Results show consistent patterns among all metrics (Figure 6). In finer detail, detrital zircon distributions are most similar to the igneous zircon distributions of their respective landmasses, for both univariate (Figure 6, left column) and bivariate (Figure 6, right column) data groups for KDE-based measures (Similarity, Likeness, and Cross-correlation). Of the 48 individual comparisons of bivariate KDEs (i.e., eight landmasses and three measures in 1D and 2D), only Cross-correlation of Baltica and Peri-Gondwana igneous and detrital zircon  $\epsilon$ HfT in 2D



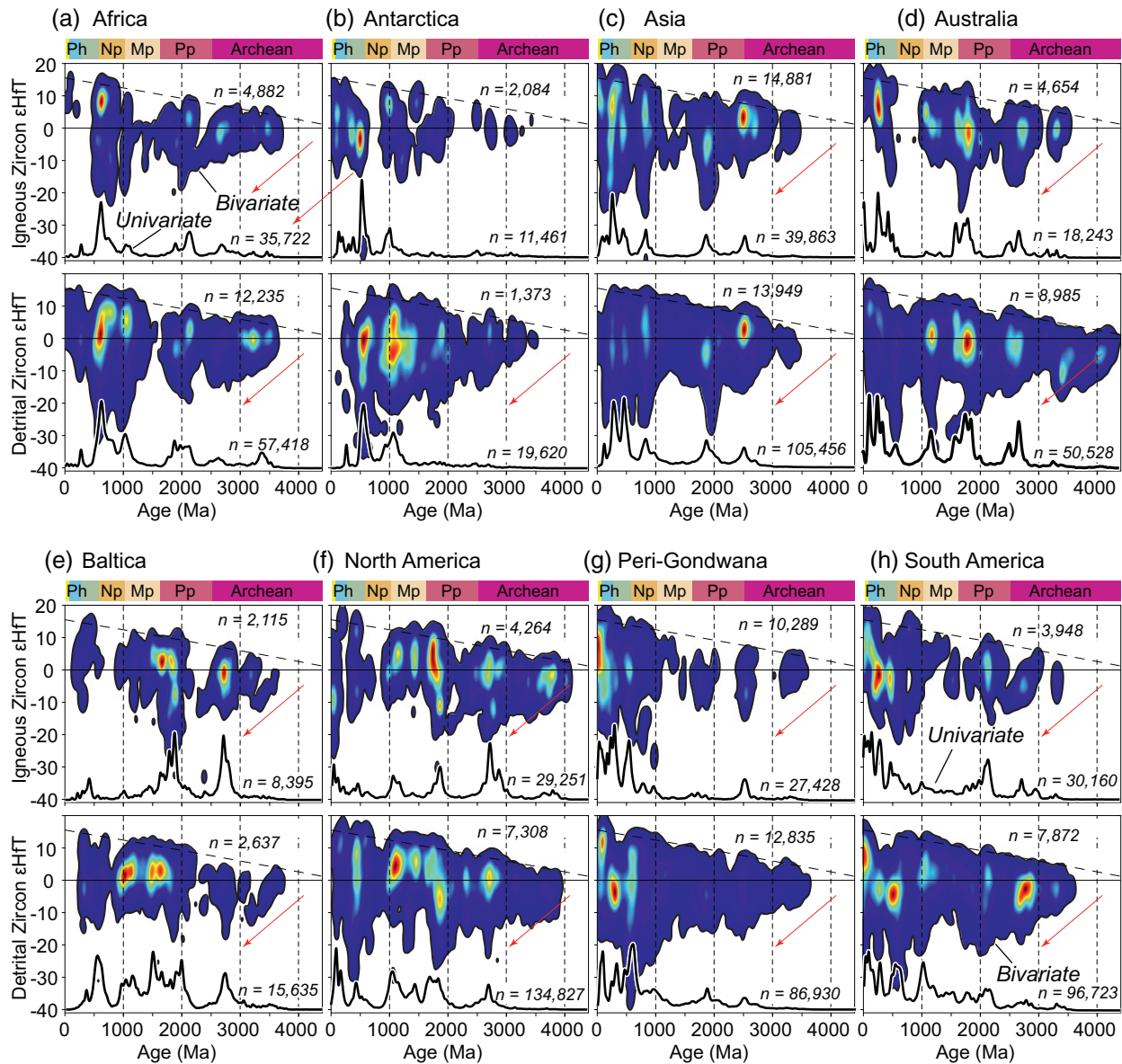


**Figure 5.** Global compilation of zircon U-Pb and  $\epsilon$ Hf data from Puetz and Condie (2019) separated into continental landmasses (a) Africa; (b) Antarctica; (c) Asia; (d) Australia, (e) Baltica; (f) North America, (g) Peri-Gondwana, (h) South America with igneous (upper panels) and detrital (lower panels) data for each group. Dashed lines are the depleted mantle array, solid horizontal lines are bulk silicate Earth chondritic reservoir, red arrows are the average crustal evolution (see Section 4 for details). KDEs were constructed with set kernel bandwidths of 40 Myr (x-axis) and  $2 \epsilon$  units (y-axis). Bivariate KDEs are clipped, that is, show white space below 99% from peak density.

are not the most similar. In contrast, fewer than half (15 of 32) of the detrital zircon distributions are most similar to their respective landmasses for CDF-based K-S and Kuiper tests, both in 1D and 2D (Figure 6).

Converting the complete comparison matrices (Supporting Information) into MDS plots produces a spatial representation of how the different paleocontinent distributions compare. In MDS plots, similar density distributions plot closer to one another and dissimilar distributions plot farther apart (Figure 7). MDS results based on 1D and 2D quantitative comparison methods show similar patterns between detrital zircon and igneous zircon for most continental landmasses. The major exceptions are Antarctica and Baltica (Figure 7). Antarctica bivariate igneous data are missing a prominent  $\sim 1,000$  Ma mode seen in the detrital bivariate data (Figure 5b). Baltica has discrepancies in both 1D and 2D. The Baltica igneous zircon U-Pb data is dominated by two age modes in the Archean and Paleoproterozoic, and the detrital distribution is complex



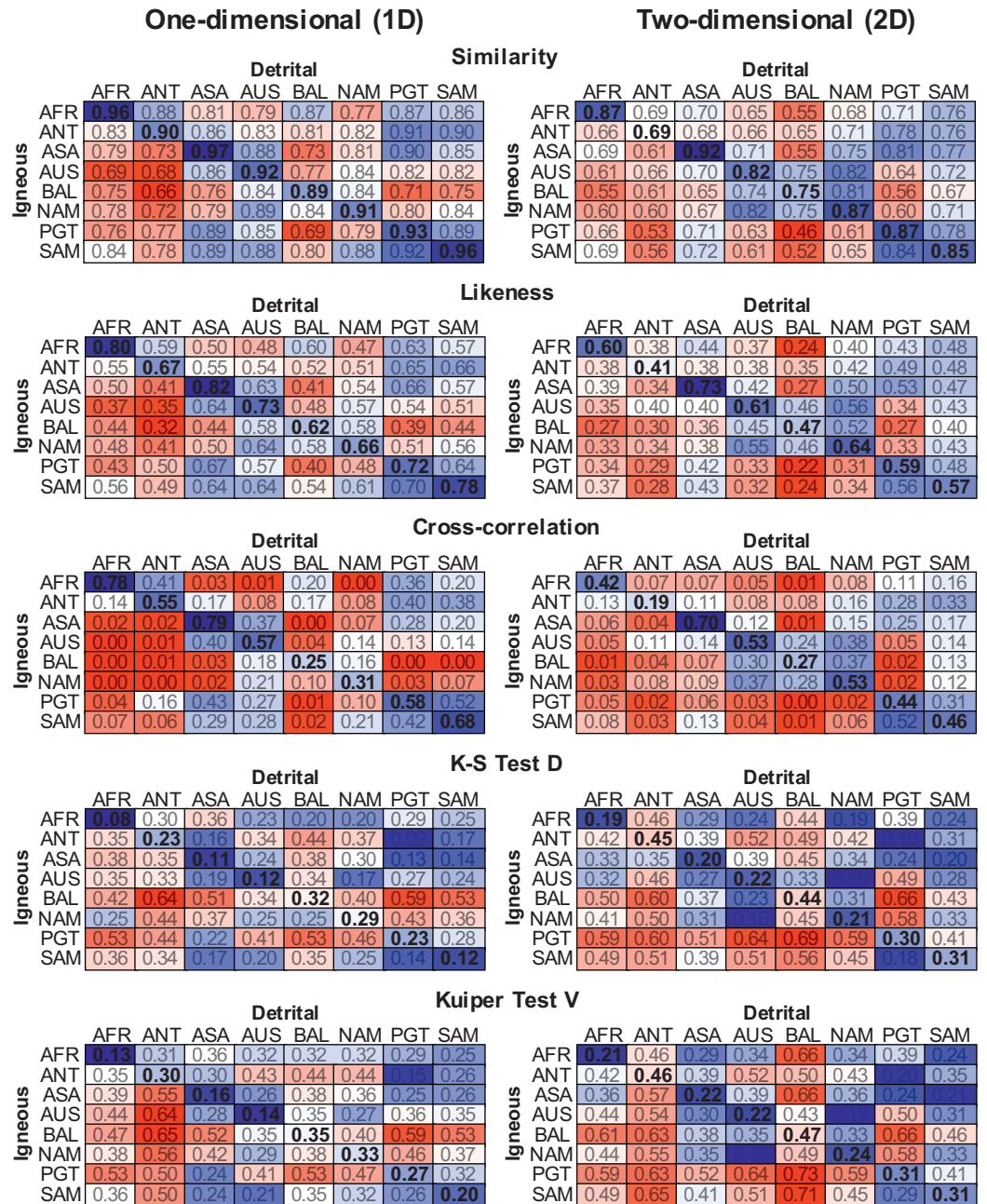
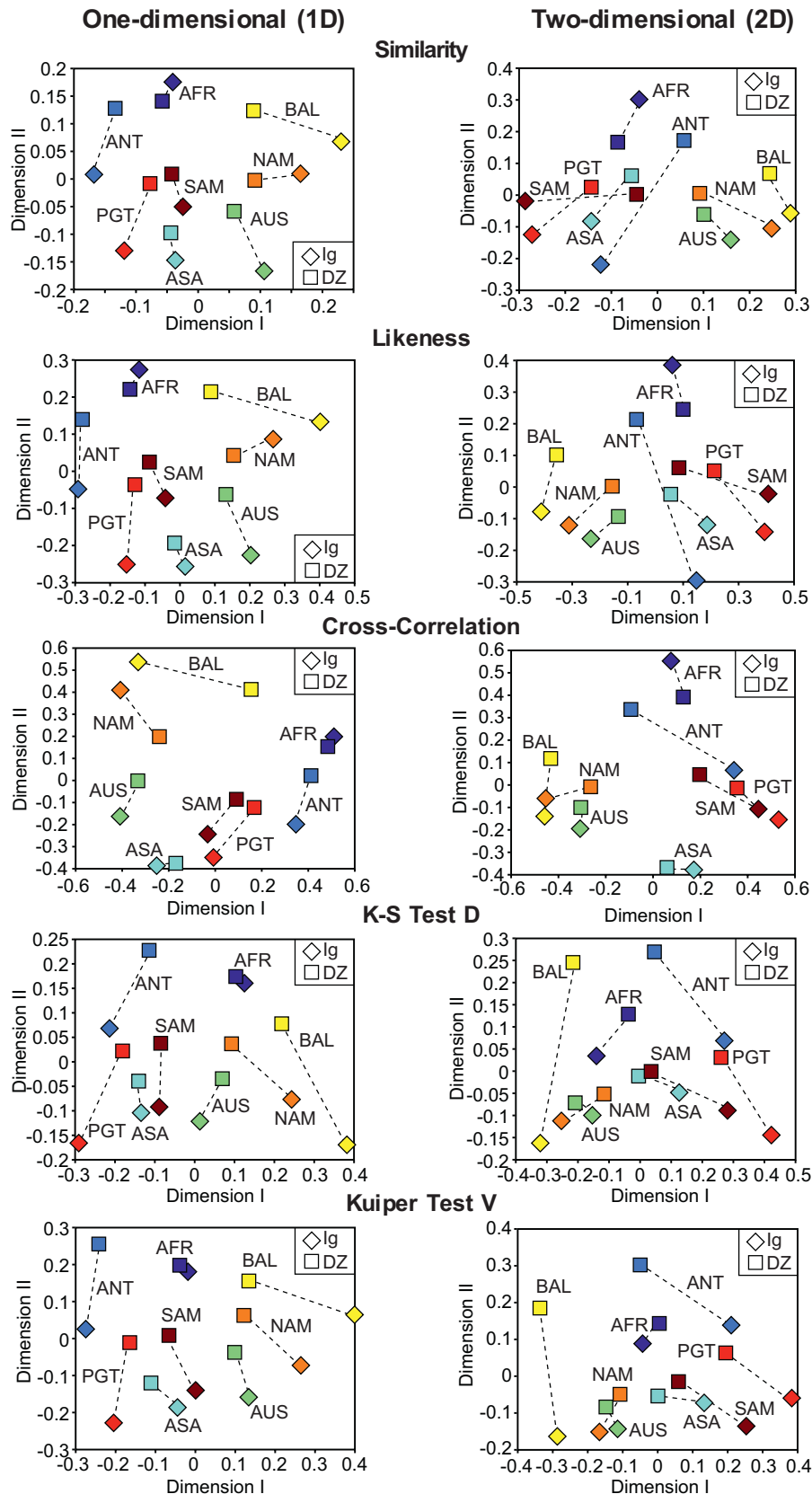


**Figure 6.** Simplified quantitative comparison results of detrital versus igneous zircon data for continental landmasses using data in Figure 5. Complete pairwise comparison matrices are presented in the Supporting Information. Each matrix is separately conditionally formatted with cooler colors representing more similar distributions and warmer colors representing less similar distributions. Note that all matrices show similar patterns both for 1D and 2D quantitative comparison methods. Also note that the most similar distributions between detrital and igneous data are for common continental landmasses for quantitative measures that use kernel density estimates (Similarity, Likeness, and Cross-correlation). AFR, Africa. ANT, Antarctica. ASA, Asia. AUS, Australia. BAL, Baltica. NAM, North America. PGT, Peri-Gondwana. SAM, South America.

and multimodal with significant Phanerozoic age contributions (Figure 5e). Baltica also shows a major ~1,000 Ma mode in the bivariate detrital distribution that is absent in the igneous distribution (Figure 5e). Continental crust is continually reworked by tectonic and sedimentary processes. Despite this, the igneous zircon record appears to be retained in the detrital record for individual paleocontinental landmasses



(Figures 5–7). Although there are commonly shared age and geochemical signals during supercontinent formation when major landmasses are adjoined due to common orogenic belts shedding detritus onto adjacent landmasses, such as the megafans of Gondwana (Squire et al., 2006), the detrital record is dominated by the bedrock igneous signal of the associated continent. Nevertheless, mixing of different sediment source terranes may exacerbate the dispersion of the detrital bivariate KDEs (Figure 5) due to the near modern paleogeographic demarcations of continental boundaries based on Paleozoic sutures used here, which do not account for earlier paleogeographic reconstructions.

#### 4.4. Is the Ediacaran-Cambrian Hf Negative Isotopic Excursion a Global Signal?

The second application of the quantitative measures to the global zircon U-Pb and Hf data compilation is on a narrower time interval over the Ediacaran-Cambrian (635–485 Ma). We chose this interval because it has been the focus of research on Earth models invoking provocative hypotheses to explain the extreme isotopic excursion to very negative  $\epsilon_{\text{HfT}}$  values. Such models posit that the excursion to negative  $\epsilon_{\text{HfT}}$  values (Figure 5) is the result of a global process such as extreme erosion during Snowball Earth and subsequent subduction of sediments generated from decreasing the continental freeboard by 1 to 3 km (Keller et al., 2019), or alternatively due to a fundamental change in plate tectonic style (Sobolev & Brown, 2019; Stern, 2008).

Visual assessment of results from the eight continental landmasses shows that univariate zircon U-Pb distributions are generally nonunique and that bivariate  $\epsilon_{\text{HfT}}$  distributions are highly variable (Figure 8). Although density modes for univariate and bivariate distributions usually occur over similar time intervals, and despite the univariate data sets being much larger, there is only minor variability in univariate space over the 150 Myr Ediacaran-Cambrian time interval, especially for detrital data (Figure 8). In contrast, bivariate  $\epsilon_{\text{HfT}}$  distributions reveal a wealth of information with major density modes that are variable in time, space (i.e., continental landmass), and geochemical deviation from depleted mantle (i.e., more positive “juvenile” or more negative “evolved”  $\epsilon_{\text{HfT}}$  values). The isotopic excursion to very negative, evolved  $\epsilon_{\text{HfT}}$  values is largely absent in all igneous distributions but is prominent in some detrital records (e.g., compare igneous and detrital records for Australia Figure 8d and the Peri-Gondwanan terranes Figure 8g). This could mean that either the sources of these zircons have not been discovered, or they were obliterated and effectively erased to all but the detrital record due to erosion, or both. At the same time, very negative  $\epsilon_{\text{HfT}}$  values are not seen in all continental detrital zircon records, challenging the notion that it is a global signal. For example,  $\epsilon_{\text{HfT}}$  values  $< -20$  are largely absent from Baltica and North America (Figures 8e–8f).

A major control on the bivariate  $\epsilon_{\text{HfT}}$  distributions is sample size. Although the igneous and detrital data groups show many similarities for associated paleocontinents, there are major discrepancies that are likely due to small sample sizes. For example, Australia, Baltica, and North America have very small sample sizes for the igneous data groups (Figures 8d–8f). For this reason, we will focus on quantitative comparison of the detrital records only.

Quantitative comparison of univariate and bivariate detrital data yields results that are consistent with visual assessments. All results are shown as MDS plots (Figure 9). The 1D comparisons, although broadly consistent with one another, reveal different patterns than the bivariate comparisons. The major differences are the relative similarity of continental masses associated with the formation of Gondwana (Africa, Antarctica, Australia, Peri-Gondwana, and South America) and those interpreted to be unassociated with Gondwana (Asia, Baltica, and North America; Goscombe et al., 2019, 2020, Figures 10a–10b). In particular, although most researchers agree that Baltica and North America were not involved in Gondwana’s formation, most of the 1D comparisons show that they are similar to Australia and South America (Figures 9 and 10a–10b; e.g., Dalla Salda, 1992; Dalziel et al., 1994; Goscombe et al., 2019, 2020; cf.; Squire et al., 2006).

A major control on the differences between Gondwanan and non-Gondwanan continental landmasses is not primarily the age modes (Figure 9, left column), but rather differences in  $\epsilon_{\text{HfT}}$ , and specifically the lack

**Figure 7.** Multidimensional scaling plots based on quantitative comparison of data presented in Figure 5 for univariate zircon U-Pb distributions with 1D quantitative comparisons (left column) and bivariate zircon  $\epsilon_{\text{HfT}}$  distributions with 2D quantitative comparisons (right column). AFR, Africa. ANT, Antarctica. ASA, Asia. AUS, Australia. BAL, Baltica. NAM, North America. PGT, Peri-Gondwana. SAM, South America. Ig, igneous zircon. DZ, detrital zircon.

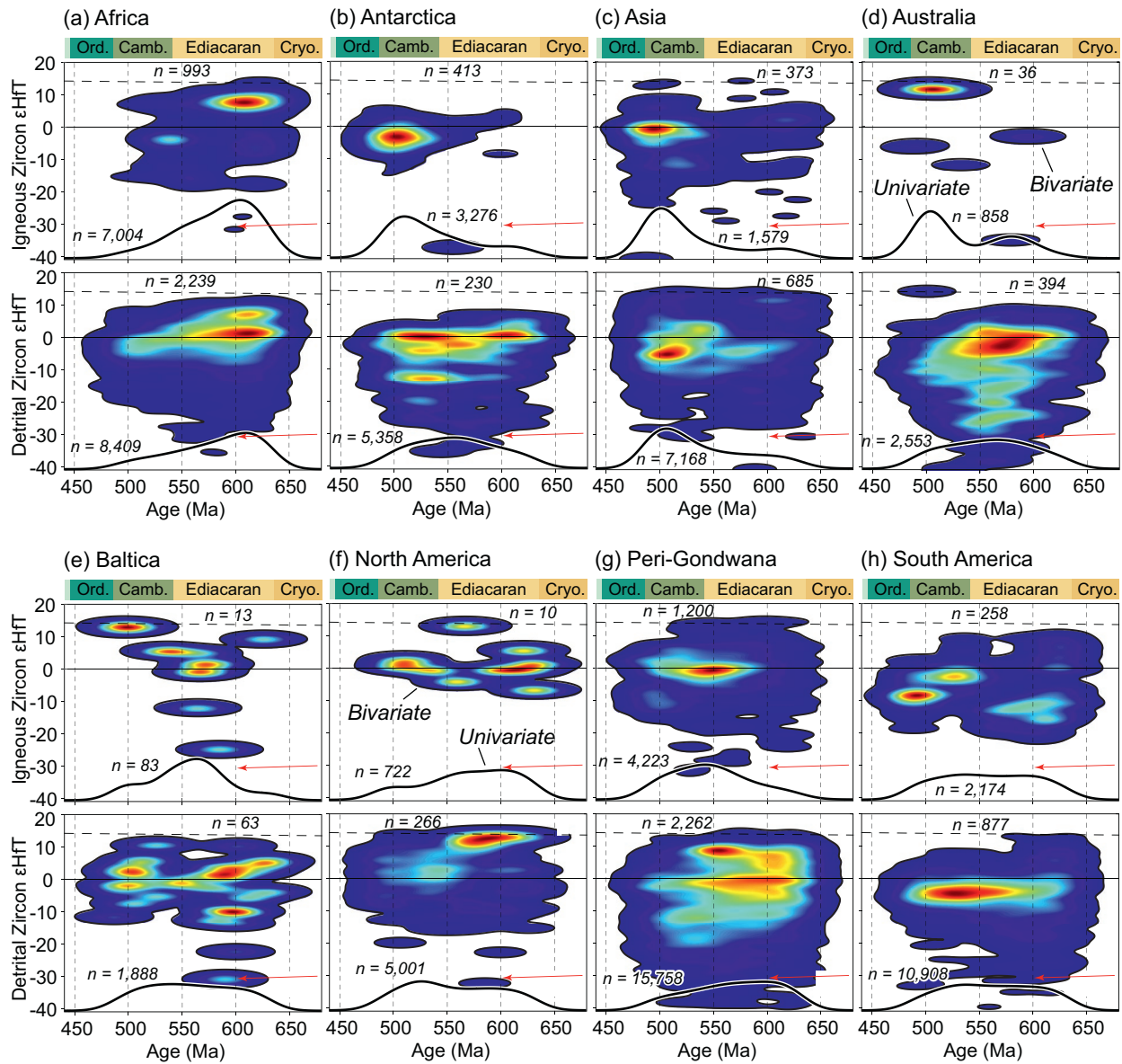
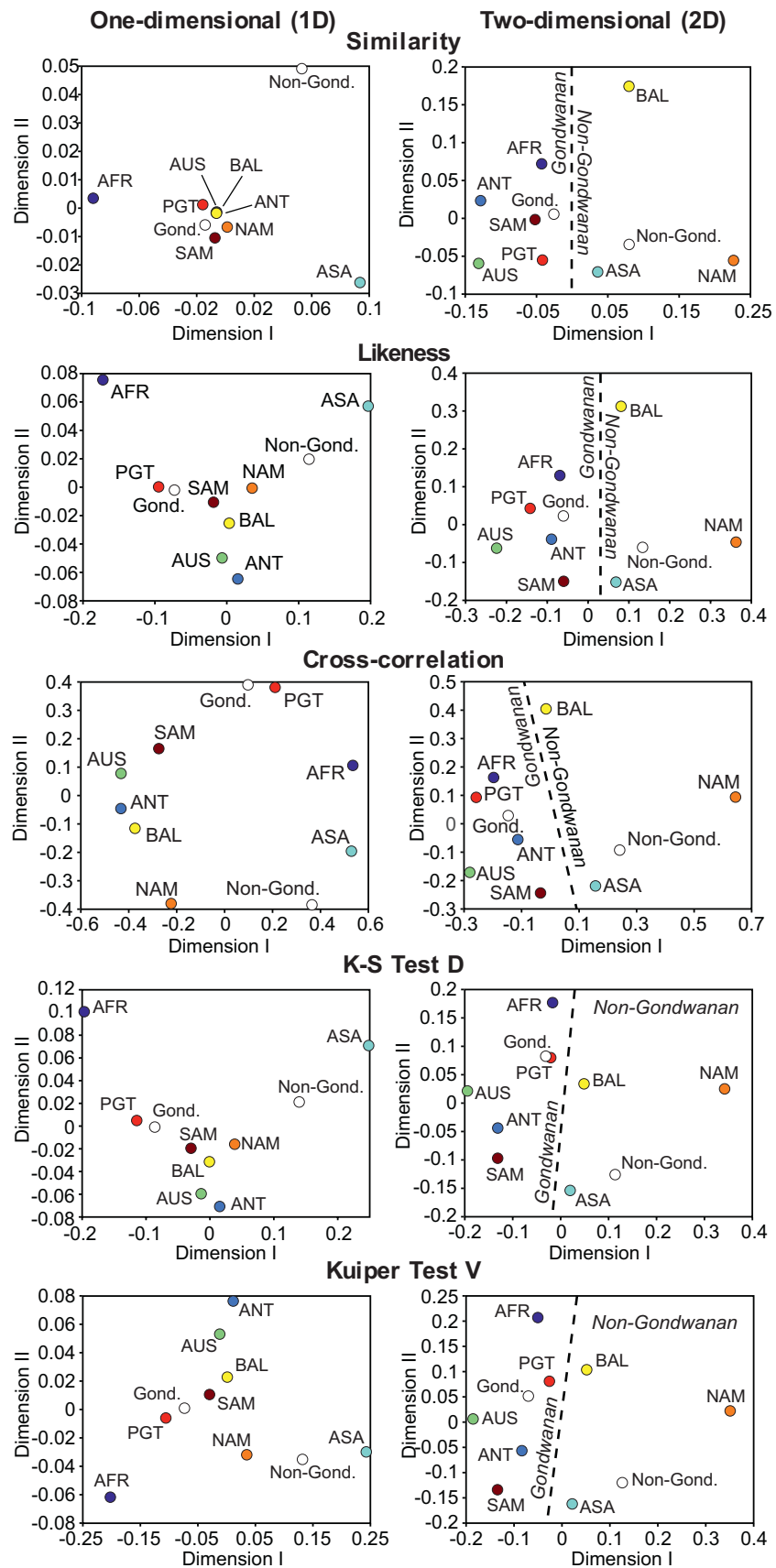


**Figure 8.** Ediacaran-Cambrian (635–485 Ma) subset of zircon U-Pb and  $\epsilon\text{HfT}$  data from Puetz and Condie (2019) separated into continental landmasses (a) Africa; (b) Antarctica; (c) Asia; (d) Australia, MAF; (e) Baltica; (f) North America, (g) Peri-Gondwana, (h) South America with igneous (upper panels) and detrital (lower panels) data for each group. Dashed lines are the depleted mantle array, solid horizontal lines are bulk silicate Earth chondritic reservoir, red arrows are the average crustal evolution (see Section 4 for details). KDEs were constructed with set kernel bandwidths of 15 Myr ( $x$ -axis) and 1  $\epsilon$  unit ( $y$ -axis). Bivariate kernel density estimates are clipped, that is, show white space below 99% from peak density.

of a major  $\epsilon\text{HfT}$  isotopic pull-down in non-Gondwanan distributions (Figure 8). This is seen in composite bivariate KDEs of Gondwanan and non-Gondwanan data (Figures 10c–10d). Calculating the intermediate Similarity step for comparison of the Gondwanan and non-Gondwanan data shows where these distributions are similar. Plotting the intermediate values as bivariate KDEs shows that they are not similar for  $\epsilon\text{HfT}$  less than  $-25$  based on intermediate  $S_{2D, \text{intermediate}}$  (Figure 10e). Accordingly, the negative  $\epsilon\text{HfT}$  isotopic excursion can be interpreted as a tectonic signal resulting from the unique paleogeography before and during the amalgamation of Gondwana, rather than a global process related to Snowball Earth erosion (Keller et al., 2019) a fundamental shift in plate tectonic regime (Sobolev & Brown, 2019; Stern, 2008), or any other wholesale global phenomenon unrelated to Gondwana.





## 5. Discussion

The data visualization and quantitative comparison methods discussed here have both strengths and weaknesses. For data visualization, bivariate KDEs facilitate identification of data clusters and can aid in objective comparison of complex bivariate data density. While bivariate CDFs are useful for quantitative comparison, they are perhaps less intuitive for visualizing data density compared to bivariate KDEs for common problems of detrital geochronology and geochemistry. One potential weakness to the methods discussed here is that neither bivariate KDEs nor CDFs incorporate sample uncertainty (cf., Vermeesch, 2012 for univariate zircon U-Pb age distributions). That said, it is possible to incorporate analytical uncertainty by altering the method to use a different Gaussian scaling matrix based on sample uncertainty for every data point in lieu of a single Gaussian scaling matrix application following conversion of data via discrete cosine transform (Ahmed et al., 1974); however, this is likely to be more computationally expensive (see Section 2.2). Another alternative is to convert Lu-Hf data to mantle extraction model ages that represent the timing of extraction from the depleted mantle (TDM; Andersen et al., 2018). This approach reduces the bivariate data into two sets of univariate data (i.e., U-Pb age and TDM) which can be plotted with uncertainty envelopes about separate CDFs (Andersen et al., 2018, their Figures 2 and 3). However, while the addition of uncertainty to univariate CDF curves is useful, the use of TDMs is problematic because they typically assume a one-stage melting model with no partial melting of older crust in a migmatite or mantle-assimilation-storage-homogenization (MASH) zone. Furthermore, the reduction of bivariate data to individual univariate data sets fundamentally decouples the two sets of information. The 2D quantitative methods outlined here allow for complete freedom in bivariate space and the preservation of coupled bivariate information.

Two-dimensional methods behave in a similar fashion to their one-dimensional counterparts in terms of sensitivity and consistency regardless of parameterization (i.e., kernel bandwidth, discretization interval). It is important to remember that all 2D quantitative comparison results are relative, as in the 1D case (Saylor & Sundell, 2016). For these reasons, it is good practice to test and compare all five quantitative methods to check for consistency among the different methods for geological interpretations. As shown in the sensitivity testing, although the results are relative, they are consistent in that they are always systematically shifted with differing parameterizations (Figure 4) and thus appear to be robust measures of similarity and dissimilarity for both univariate and bivariate distributions. In practice, if one or more methods gives a drastically different result, particularly between KDE-based and CDF-based measures, then the results are likely not as reliable; the most robust quantitative assessments should be broadly consistent regardless of the method used. More importantly, quantitative comparison results should always be thoroughly scrutinized by comparison to independent geologic observations and interpretations (e.g., stratigraphic stacking patterns, cross-cutting relationships). As with all model-based results, they are ancillary to real-world observations and should only be applied with a proper characterization and understanding of geologic context.

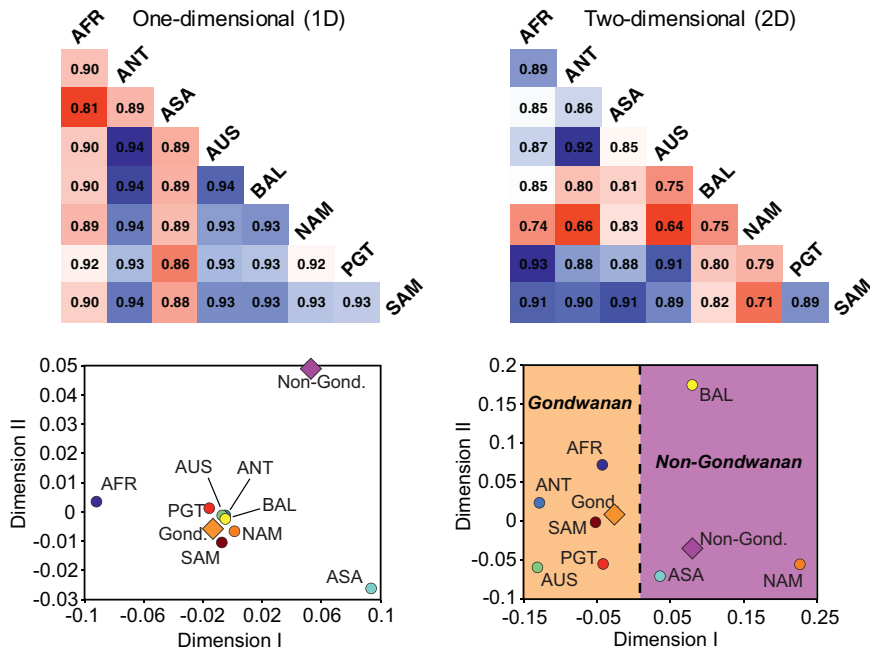
The 2D quantitative comparison methods of bivariate KDEs and CDFs as applied to the complete temporal  $\epsilon$ HfT compilation highlights weaknesses in the K-S and Kuiper tests, both for univariate and bivariate data. Visual assessment shows that univariate U-Pb modes and bivariate  $\epsilon$ HfT modes generally align for igneous zircon and detrital zircon records of individual landmasses (Figure 5). All measures show similar trends in 1D and 2D for detrital and igneous zircon records (Figure 6 and Supporting Information). However, results for KDE-based measures (Similarity, Likeness, Cross-correlation) are more consistent (only 46 out of 48) in that they show the detrital zircon records are most similar to the igneous records of their respective continental landmass (Figure 5). On the other hand, the K-S Test and Kuiper Test are much less consistent in both 1D and 2D, with only 15 of 32 comparisons showing the igneous and detrital records are the most similar for common landmasses. We attribute the discrepancies in CDF-based measures to roughly equal vertical separation (i.e., D or V values) between CDFs with modes at similar intervals, even if there is no overlap between the modes, which results in lower sensitivity to the details of density distributions (Figure 4).

The geological applications of 2D quantitative comparison methods presented here are consistent with many of the proof-of-concept results shown in Figure 1 and the sensitivity testing results shown in Figure 4.

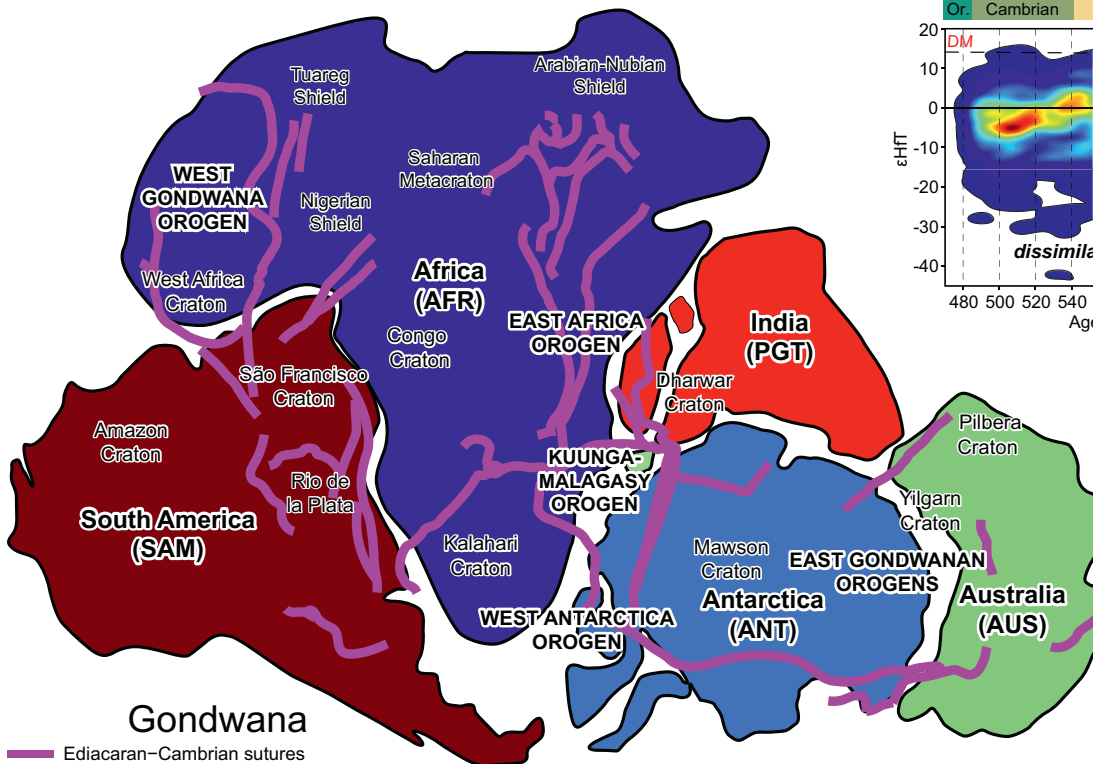
**Figure 9.** Multidimensional scaling plots based on quantitative comparison of data presented in Figure 8 for univariate zircon U-Pb distributions with 1D quantitative comparisons (left column) and bivariate zircon  $\epsilon$ HfT distributions with 2D quantitative comparisons (right column). AFR, Africa. ANT, Antarctica. ASA, Asia. AUS, Australia. BAL, Baltica. NAM, North America. PGT, Peri-Gondwana. SAM, South America.



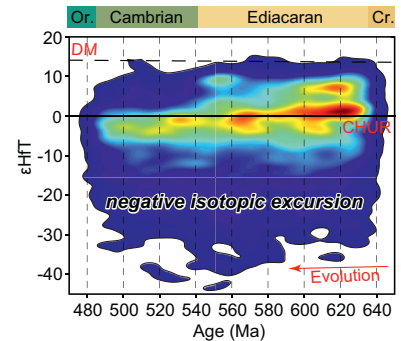
(a) Comparison matrices and corresponding MDS plots



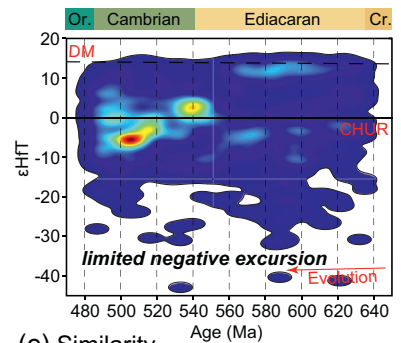
(b) Paleogeographic reconstruction of Gondwana



(c) Gondwanan Composite



(d) Non-Gondwanan Composite



(e) Similarity

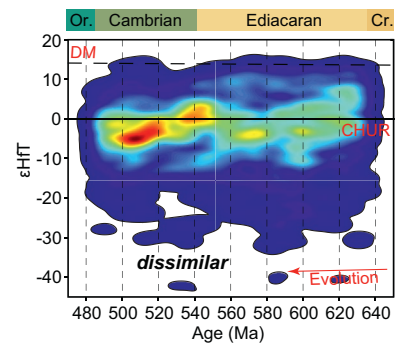


**Figure 10.** (a) Color-coded pairwise comparison matrices based on 1D (left) and 2D (right) Similarity from Figure 9. AFR, Africa. ANT, Antarctica. ASA, Asia. AUS, Australia. BAL, Baltica. NAM, North America. PGT, Peri-Gondwana. SAM, South America. (b) Ediacaran-Cambrian paleogeographic reconstruction of Gondwana with regional orogenic belts, cratons, and suture locations from Goscombe et al. (2019). (c) Composite Gondwanan terranes (Africa + Antarctica + Australia + Peri-Gondwana + South America). (d) Composite non-Gondwanan terranes (Asia + Baltica + North America). (e) Intermediate step in calculating Similarity before summing which shows where the two composite  $\epsilon\text{HfT}$  distributions in parts c and d are similar. Bivariate KDEs in parts (c)–(e) were constructed with set kernel bandwidths of 5 Myr (x-axis) and 1  $\epsilon$  unit (y-axis).

For example, the 2D metrics behave similarly to their 1D counterparts, as shown with the comparison of the complete detrital and igneous zircon records (i.e., 4,400–0 Ma; Figures 5–7). Perhaps more interestingly, the 2D approach to the Ediacaran-Cambrian data reveals dramatically different results compared to the 1D quantitative assessments (Figures 8–10). The latter result is by design and demonstrates with empirical data how univariate age distributions can be nonunique and can potentially produce misleading results. These results highlight the importance of thoroughly scrutinizing any model-based results to ensure that they are appropriately interpreted in geologic context.

The 2D quantitative comparison methods hold promise for detrital applications where univariate zircon U-Pb age distributions are nonunique due to overlapping age groups. Here we have demonstrated the utility of 2D quantitative comparison methods using paired zircon U-Pb and Hf data, as it has not only become common in sediment provenance studies (e.g., Gehrels & Pecha, 2014) but it has also become a major lens to interpret secular changes in crustal growth, global erosion, and changes in tectonic styles (e.g., Belousova et al., 2010). The future is bright for 2D quantitative assessment, as incorporating a second dimension of information for detrital minerals is becoming more common using thermochronology (Reiners et al., 2005; Saylor et al., 2013), trace element geochemistry (e.g., Anfinson et al., 2016; McKenzie et al., 2018), as well as physical characteristics of zircon such as grain roundness (Decou et al., 2013; Sundell et al., 2018) or grain size (Leary et al., 2020). Moreover, the 2D methods described above are not limited to detrital applications. They can be used to compare any bivariate data that can appropriately be visualized in terms of density and represented as a bivariate KDE. Similar to 1D methods of quantitative comparison, 2D methods have major applications in exploratory research, and future work may involve implementation of mixture model approaches currently implemented for univariate distributions (e.g., Galbraith & Green, 1990; Sambridge & Compston, 1994; Sundell & Saylor, 2017). As the study of Earth Science continues head on into the realm of “big data” (e.g., Guo, 2017; Sellars et al., 2013; Vermeesch & Garzanti, 2015), and geochronology and geochemistry data aggregation initiatives progress (e.g., Quinn et al., 2020), development of tools for exploratory data analysis in the Earth Sciences is seemingly more important than ever.

## 6. *DZstats2D* Software

We implemented the 2D quantitative methods into a new MATLAB-based program, *DZstats2D*. The program reads sample spreadsheets containing paired columns of bivariate data. Although *DZstats2D* is by default parameterized to plot and compare age and Hf data, it is capable of comparing any bivariate data that can be meaningfully visualized in bivariate sample space as a KDE. The *DZstats2D* code is open source and has been deployed as stand-alone desktop applications for macOS and Windows. The code, applications, and all data discussed in this contribution are available at on GitHub at <https://github.com/kurtsundell/DZstats2D>. An example step-by-step guide to exploratory analysis is included in the *DZstats2D* software user manual.

## 7. Conclusions

We present 2D quantitative comparison methods applied to zircon U-Pb and Hf data. The 2D measures are simple mathematical extensions of their 1D counterparts commonly applied to univariate detrital zircon U-Pb age distributions: Similarity, Likeness, and Cross-correlation of KDEs and K-S Test and Kuiper Test of CDFs. Sensitivity testing shows that the 2D measures behave in a similar fashion to their 1D counterparts in terms of sensitivity; parameterization such as kernel bandwidth and discretization interval have only a minor effect on results by systematically shifting all measures, which suggests that the 2D quantitative methods are robust. Application to a global compilation of U-Pb and Hf data parsed geographically into major continental landmasses shows that detrital zircon records are most similar to the igneous zircon records from the same landmass, suggesting that the detrital zircon record provides a faithful representation of the igneous record. Comparison of Ediacaran-Cambrian records reveals that consideration of only univariate zircon U-Pb ages for 1D quantitative comparison produces misleading results. Consideration of a second data dimension shows that there is considerable variability in the Hf data and that samples fall into Gondwanan and non-Gondwanan groups. The latter also highlights that the Ediacaran-Cambrian isotopic excursion to evolved values is likely not a global signal, but rather a tectonic signal associated only

with continental fragments involved in the amalgamation of Gondwana. The methods presented in this manuscript are implemented in a new MATLAB-based graphical user interface, *DZstats2D*, available as open-source code and as standalone applications for macOS and Windows.

### Data Availability Statement

Data used in this research were originally compiled and are available from Puetz and Condie (2019) and are also available at <https://zenodo.org/badge/latestdoi/313485301>, DOI: <http://doi.org/10.5281/zenodo.4460336>, along with the latest version of *DZstats2D*.

### Acknowledgments

The authors are grateful to Christopher Spencer and one anonymous reviewer for thorough and constructive comments, as well as Editor Peter van der Beek for manuscript handling. We thank Francis Macdonald for enlightening discussions on the application and interpretation of Hf data and the Ediacaran-Cambrian reconstruction of Gondwana. We thank Steve Puetz and Kent Condie for compiling the global database of zircon U-Pb and Hf data, and all who made their data publicly available. The authors thank George Gehrels, Mark Pecha, Nicky Giesler, Martin Pepper, Sarah George, and Federico Moreno at the Arizona LaserChron Center (ALC); and Mark Holland for discussion on quantitative methods and potential Earth Science applications. This work was partially funded by the National Science Foundation grant EAR-1649254 to Gehrels and Ruiz for the ALC in support of KES.

### References

Ahmed, N., Natarajan, T., & Rao, K. R. (1974). Discrete cosine transform. *IEEE Transactions on Computers*, *100*, 90–93.

Amidon, W. H., Burbank, D. W., & Gehrels, G. E. (2005). Construction of detrital mineral populations: Insights from mixing of U–Pb zircon ages in Himalayan rivers. *Basin Research*, *17*(4), 463–485. <https://doi.org/10.1111/bre.12245>

Andersen, T. (2014). The detrital zircon record: Supercontinents, parallel evolution—Or coincidence? *Precambrian Research*, *244*, 279–287.

Andersen, T., Kristoffersen, M., & Elburg, M. A. (2018). Visualizing, interpreting and comparing detrital zircon age and Hf isotope data in basin analysis—A graphical approach. *Basin Research*, *30*(1), 132–147.

Anfinson, O. A., Malusà, M. G., Ottria, G., Dafov, L. N., & Stockli, D. F. (2016). Tracking coarse-grained gravity flows by LASS-ICP-MS depth-profiling of detrital zircon (Aveto Formation, Adriatic foredeep, Italy). *Marine and Petroleum Geology*, *77*, 1163–1176.

Belousova, E. A., Kostitsyn, Y. A., Griffin, W. L., Begg, G. C., O'Reilly, S. Y., & Pearson, N. J. (2010). The growth of the continental crust: Constraints from zircon Hf-isotope data. *Lithos*, *119*(3–4), 457–466. <https://doi.org/10.1016/j.lithos.2010.07.024>

Bhattacharyya, A. (1943). On a measure of divergence between two statistical populations defined by their probability distributions. *Bulletin of the Calcutta Mathematical Society*, *35*, 99–109.

Böhme, M., Spassov, N., Ebner, M., Geraads, D., Hristova, L., Kirscher, U., et al. (2017). Messinian age and savannah environment of the possible hominin *Graecopithecus* from Europe. *PLoS One*, *12*. e0177347. <https://doi.org/10.1371/journal.pone.0177347>

Botev, Z. I., Grotowski, J. F., & Kroese, D. P. (2010). Kernel density estimation via diffusion. *Annals of Statistics*, *38*, 2916–2957. <https://doi.org/10.1214/10-AOS799>

Cherniak, D. J., Hanchar, J. M., & Watson, E. B. (1997). Diffusion of tetravalent cations in zircon. *Contributions to Mineralogy and Petrology*, *127*, 383–390.

Cohen, J. (1977). *Statistical Power Analysis for the Behavioral Sciences*, New York, NY: Academic Press New York.

Dalla Salda, L. H., Dalziel, I. W., Cingolani, C. A., & Varela, R. (1992). Did the Taconic Appalachians continue into southern South America? *Geology*, *20*, 1059–1062.

Dalziel, I. W. (1994). Precambrian Scotland as a Laurentia-Gondwana link: Origin and significance of cratonic promontories. *Geology*, *22*, 589–592.

Decou, A., Von Eynatten, H., Dunkl, I., Frei, D., & Wörner, G. (2013). Late Eocene to Early Miocene Andean uplift inferred from detrital zircon fission track and U–Pb dating of Cenozoic forearc sediments (15–18 S). *Journal of South American Earth Sciences*, *45*, 6–23. <https://doi.org/10.1016/j.jsames.2013.02.003>

Dickinson, W. R., & Gehrels, G. E. (2009). Use of U–Pb ages of detrital zircons to infer maximum depositional ages of strata: A test against a Colorado Plateau Mesozoic database. *Earth and Planetary Science Letters*, *288*, 115–125. <https://doi.org/10.1016/j.epsl.2009.09.013>

Dodson, M. H., Compston, W., Williams, I. S., & Wilson, J. F. (1988). A search for ancient detrital zircons in Zimbabwean sediments. *Journal of the Geological Society*, *145*, 977–983.

Domeier, M., & Torsvik, T. H. (2014). Plate tectonics in the late Paleozoic. *Geoscience Frontiers*, *5*, 303–350. <https://doi.org/10.1016/j.gsf.2014.01.002>

Galbraith, R. F., & Green, P. F. (1990). Estimating the component ages in a finite mixture. *International Journal of Radiation Applications and Instrumentation*, *17*, 197–206.

Gehrels, G., & Pecha, M. (2014). Detrital zircon U–Pb geochronology and Hf isotope geochemistry of Paleozoic and Triassic passive margin strata of western North America. *Geosphere*, *10*(1), 49–65. <https://doi.org/10.1130/GES00889.1>

Gehrels, G. E. (2000). Introduction to detrital zircon studies of Paleozoic and Triassic strata in western Nevada and northern California. *Special Papers – Geological Society of America*, *347*, 1–17.

Gehrels, G. E., Dickinson, W. R., Ross, G. M., Stewart, J. H., & Howell, D. G. (1995). Detrital zircon reference for Cambrian to Triassic miogeoclinal strata of western North America. *Geology*, *23*, 831–834.

Goscombe, B., Foster, D. A., Blewett, R., Czarnota, K., Wade, B., Groenewald, B., & Gray, D. (2019). Neoproterozoic metamorphic evolution of the Yilgarn Craton: A record of subduction, accretion, extension and lithospheric delamination. *Precambrian Research*, *335*, 105441. <https://doi.org/10.1016/j.precamres.2019.105441>

Goscombe, B., Foster, D. A., Gray, D., & Wade, B. (2020). Assembly of central Gondwana along the Zambezi Belt: Metamorphic response and basement reactivation during the Kuunga Orogeny. *Gondwana Research*, *80*, 410–465. <https://doi.org/10.1016/j.gr.2019.11.004>

Griffin, W. L., Pearson, N. J., Belousova, E., Jackson, S. V., Van Achterbergh, E., O'Reilly, S. Y., & Shee, S. R. (2000). The Hf isotope composition of cratonic mantle: LAM-MC-ICPMS analysis of zircon megacrysts in kimberlites. *Geochimica et Cosmochimica Acta*, *64*, 133–147.

Guo, H. (2017). Big Earth data: A new frontier in Earth and information sciences. *Big Earth Data*, *1*(1–2), 4–20.

Hoskin, P. W., & Ireland, T. R. (2000). Rare earth element chemistry of zircon and its use as a provenance indicator. *Geology*, *28*, 627–630.

Hubbard, R. (2019). Will the ASA's efforts to improve statistical practice be successful? Some evidence to the contrary. *The American Statistician*, *73*, 31–35. <https://doi.org/10.1080/00031305.2018.1497540>

Keller, C. B., Husson, J. M., Mitchell, R. N., Bottke, W. F., Gernon, T. M., Boehnke, P., et al. (2019). Neoproterozoic glacial origin of the great unconformity. *Proceedings of the National Academy of Sciences*, *116*, 1136–1145. <https://doi.org/10.1073/pnas.1804350116>

Kruskal, J. B. (1964). Nonmetric multidimensional scaling: a numerical method. *Psychometrika*, *29*, 115–129.

Kuiper, N. H. (1960). *Tests concerning random points on a circle*, paper presented at Indagationes Mathematicae (Proceedings). Elsevier.

- Leary, R. J., Smith, M. E., & Umhoefer, P. (2020). Grain-size control on detrital zircon cycloprovenance in the Late Paleozoic Paradox and Eagle Basins, USA. *Journal of Geophysical Research: Solid Earth*, *125*, 1–19. <https://doi.org/10.1029/2019JB019226>
- Massey, F. J., Jr. (1951). The Kolmogorov-Smirnov test for goodness of fit. *Journal of the American Statistical Association*, *46*, 68–78.
- McKenzie, N. R., Horton, B. K., Loomis, S. E., Stockli, D. F., Planavsky, N. J., & Lee, C. T. A. (2016). Continental arc volcanism as the principal driver of icehouse-greenhouse variability. *Science*, *352*, 444–447. <https://doi.org/10.1126/science.aad5787>
- McKenzie, N. R., Smye, A. J., Hegde, V. S., & Stockli, D. F. (2018). Continental growth histories revealed by detrital zircon trace elements: A case study from India. *Geology*, *46*, 275–278. <https://doi.org/10.1130/G39973.1>
- Metcalfe, I. (2013). Gondwana dispersion and Asian accretion: Tectonic and palaeogeographic evolution of eastern Tethys. *Journal of Asian Earth Sciences*, *66*, 1–33. <https://doi.org/10.1016/j.jseas.2012.12.020>
- Miller, M. B. (2014). *Mathematics and statistics for financial risk management* (2nd ed.). Hoboken, NJ: John Wiley and Sons, Inc.
- Peacock, J. A. (1983). Two-dimensional goodness-of-fit testing in astronomy. *Monthly Notices of the Royal Astronomical Society*, *202*, 615–627.
- Pearson, R. K. (2011). *Exploring data in engineering, the sciences, and medicine*. New York, NY: Oxford University Press.
- Press, W. H., & Teukolsky, S. A. (1988). Kolmogorov-Smirnov Test for Two-Dimensional Data: How to tell whether a set of (x,y) data points are consistent with a particular probability distribution, or with another data set. *Computers in Physics*, *2*, 74–77.
- Puetz, S. J., & Condie, K. C. (2019). Time series analysis of mantle cycles Part I: Periodicities and correlations among seven global isotopic databases. *Geoscience Frontiers*, *10*(4), 1305–1326. <https://doi.org/10.1016/j.gsf.2019.04.002>
- Pullen, A., Ibáñez-Mejía, M., Gehrels, G. E., Ibáñez-Mejía, J. C., & Pecha, M. (2014). What happens when n = 1000? Creating large-n geochronological datasets with LA-ICP-MS for geologic investigations. *Journal of Analytical Atomic Spectrometry*, *29*, 971–980. <https://doi.org/10.1039/c4ja00024b>
- Quinn, D. P., Linzmeier, B. J., Sundell, K. E., Bruck, B. T., Ye, S., Gehrels, G. G., et al. (2020). *The Sparrow software interface for linking analytical data and metadata in laboratory archives*. San Diego, CA: EarthCube Annual Meeting.
- Reiners, P. W. (2005). Zircon (U-Th)/He thermochronometry. *Reviews in Mineralogy and Geochemistry*, *58*(1), 151–179. <https://doi.org/10.2138/rmg.2005.58.6>
- Roberts, N. M. (2012). Increased loss of continental crust during supercontinent amalgamation. *Gondwana Research*, *21*, 994–1000. <https://doi.org/10.1016/j.gr.2011.08.001>
- Roberts, N. M., & Spencer, C. J. (2015). The zircon archive of continent formation through time. *Geological Society, London, Special Publications*, *389*(1), 197–225. <http://dx.doi.org/10.1144/SP389.14>
- Sambridge, M. S., & Compston, W. (1994). Mixture modeling of multi-component data sets with application to ion-probe zircon ages. *Earth and Planetary Science Letters*, *128*, 373–390. [https://doi.org/10.1016/0012-821X\(94\)90157-0](https://doi.org/10.1016/0012-821X(94)90157-0)
- Satkoski, A. M., Wilkinson, B. H., Hietpas, J., & Samson, S. D. (2013). Likeness among detrital zircon populations—An approach to the comparison of age frequency data in time and space. *The Geological Society of America Bulletin*, *125*, 1783–1799. <http://dx.doi.org/10.1144/SP389.14>
- Saylor, J. E., Knowles, J. N., Horton, B. K., Nie, J., & Mora, A. (2013). Mixing of source populations recorded in detrital zircon U-Pb age spectra of modern river sands. *The Journal of Geology*, *121*, 17–33. <https://doi.org/10.1086/668683>
- Saylor, J. E., & Sundell, K. E. (2016). Quantifying comparison of large detrital geochronology data sets. *Geosphere*, *12*, 203–220. <https://doi.org/10.1130/GES01237.1>
- Saylor, J. E., Sundell, K. E., & Sharman, G. R. (2019). Characterizing sediment sources by non-negative matrix factorization of detrital geochronological data. *Earth and Planetary Science Letters*, *512*, 46–58. <https://doi.org/10.1016/j.epsl.2019.01.044>
- Schärer, U., & Allègre, C. J. (1982). Investigation of the Archean crust by single-grain dating of detrital zircon: A greywacke of the Slave Province, Canada. *Canadian Journal of Earth Sciences*, *19*, 1910–1918.
- Sellars, S., Nguyen, P., Chu, W., Gao, X., Hsu, K. L., & Sorooshian, S. (2013). Computational Earth science: Big data transformed into insight. *Eos, Transactions American Geophysical Union*, *94*(32), 277–278.
- Sharman, G. R., & Johnstone, S. A. (2017). Sediment unmixing using detrital geochronology. *Earth and Planetary Science Letters*, *477*, 183–194. <https://doi.org/10.1016/j.epsl.2017.07.044>
- Silverman, B. W. (1986). *Density estimation for statistics and data analysis*. London: Chapman and Hall.
- Sobolev, S. V., & Brown, M. (2019). Surface erosion events controlled the evolution of plate tectonics on earth. *Nature*, *570*, 52–57. <https://doi.org/10.1038/s41586-019-1258-4>
- Söderlund, U., Patchett, P. J., Vervoort, J. D., & Isachsen, C. E. (2004). The <sup>176</sup>Lu decay constant determined by Lu–Hf and U–Pb isotope systematics of Precambrian mafic intrusions. *Earth and Planetary Science Letters*, *219*, 311–324. [https://doi.org/10.1016/S0012-821X\(04\)00012-3](https://doi.org/10.1016/S0012-821X(04)00012-3)
- Speer, J. A. (1980). Zircon. *Reviews in Mineralogy and Geochemistry*, *5*, 67–112.
- Spencer, C. J., Dyck, B., Mottram, C. M., Roberts, N. M., Yao, W. H., & Martin, E. L. (2019). Deconvolving the pre-Himalayan Indian margin—tales of crustal growth and destruction. *Geoscience Frontiers*, *10*, 863–872. <https://doi.org/10.1016/j.gsf.2018.02.007>
- Squire, R. J., Campbell, I. H., Allen, C. M., & Wilson, C. J. (2006). Did the Transgondwanan Supermountain trigger the explosive radiation of animals on earth? *Earth and Planetary Science Letters*, *250*, 116–133. <https://doi.org/10.1016/j.epsl.2006.07.032>
- Stacey, J. T., & Kramers, J. D. (1975). Approximation of terrestrial lead isotope evolution by a two-stage model. *Earth and Planetary Science Letters*, *26*, 207–221.
- Stern, R. J. (2008). Modern-style plate tectonics began in Neoproterozoic time: An alternative interpretation of Earth's tectonic history. *When Did Plate Tectonics Begin on Planet Earth*, 265, 280.
- Stockli, D. F. (2005). Application of low-temperature thermochronometry to extensional tectonic settings. *Reviews in Mineralogy and Geochemistry*, *58*, 411–448. <https://doi.org/10.2138/rmg.2005.58.16>
- Sundell, K. E., Gehrels, G. E., & Pecha, M. E. (2020). *Rapid U-Pb geochronology by laser ablation multi-collector ICP-MS*. Geostandards and Geoanalytical Research. <https://doi.org/10.1111/ggr.12355>
- Sundell, K. E., & Saylor, J. E. (2017). Unmixing detrital geochronology age distributions. *Geochemistry, Geophysics, Geosystems*, *18*, 2872–2886. <https://doi.org/10.1002/2016GC006774>
- Sundell, K. E., Saylor, J. E., Lapen, T. J., Styron, R. H., Villarreal, D. P., Usnayo, P., & Cárdenas, J. (2018). Peruvian Altiplano stratigraphy highlights along-strike variability in foreland basin evolution of the Cenozoic central Andes. *Tectonics*, *37*, 1876–1904. <https://doi.org/10.1029/2017TC004775>
- Tatsumoto, M., & Patterson, C. (1964). Age studies of zircon and feldspar concentrates from the Franconia sandstone. *The Journal of Geology*, *72*, 232–242. <https://doi.org/10.1086/626978>



- Thomas, W. A., Gehrels, G. E., Sundell, K. E., Greb, S. F., Finzel, E. S., Clark, R. J., et al. (2020). Detrital zircons and sediment dispersal in the eastern Midcontinent of North America. *Geosphere*, *16*, 817–843. <https://doi.org/10.1130/GES02152.1>
- Tucker, R. T., Roberts, E. M., Hu, Y., Kemp, A. I., & Salisbury, S. W. (2013). Detrital zircon age constraints for the Winton Formation, Queensland: Contextualizing Australia's Late Cretaceous dinosaur faunas. *Gondwana Research*, *24*, 767–779. <https://doi.org/10.1016/j.gr.2012.12.009>
- Tye, A. R., Wolf, A. S., & Niemi, N. A. (2019). Bayesian population correlation: A probabilistic approach to inferring and comparing population distributions for detrital zircon ages. *Chemical Geology*, *518*, 67–78. <https://doi.org/10.1016/j.chemgeo.2019.03.039>
- Vermeesch, P. (2004). How many grains are needed for a provenance study? *Earth and Planetary Science Letters*, *224*, 441–451. <https://doi.org/10.1016/j.epsl.2004.05.037>
- Vermeesch, P. (2012). On the visualisation of detrital age distributions. *Chemical Geology*, *312*, 190–194. <https://doi.org/10.1016/j.chemgeo.2012.04.021>
- Vermeesch, P. (2013). Multi-sample comparison of detrital age distributions. *Chemical Geology*, *341*, 140–146. <https://doi.org/10.1016/j.chemgeo.2013.01.010>
- Vermeesch, P. (2018). Dissimilarity measures in detrital geochronology. *Earth-Science Reviews*, *178*, 310–321. <https://doi.org/10.1016/j.earscirev.2017.11.027>
- Vermeesch, P. (2020). Maximum depositional age estimation revisited. *Geoscience Frontiers*, *12*, 843–850. <https://doi.org/10.1016/j.gsf.2020.08.008>
- Vermeesch, P., & Garzanti, E. (2015). Making geological sense of “Big Data” in sedimentary provenance analysis. *Chemical Geology*, *409*, 20–27. <https://doi.org/10.1016/j.chemgeo.2015.05.004>
- Vervoort, J. D., & Blichert-Toft, J. (1999). Evolution of the depleted mantle: Hf isotope evidence from juvenile rocks through time. *Geochimica et cosmochimica acta*, *63*(3–4), 533–556.
- Wasserstein, R. L., Schirm, A. L., & Lazar, N. A. (2019). Moving to a world beyond “ $p < 0.05$ ”. *The American Statistician*, *73*, 1–19. <https://doi.org/10.1080/00031305.2019.1583913>